RESEARCH ARTICLE

WILEY

On a novel full decoupling, linear, second-order accurate, and unconditionally energy stable numerical scheme for the anisotropic phase-field dendritic crystal growth model

Xiaofeng Yang[ORCID]

Department of Mathematics, University of South Carolina, Columbia, South Carolina, USA

Correspondence
Xiaofeng Yang, Department of Mathematics, University of South Carolina, Columbia, SC 29208, USA.
Email: xfyang@math.sc.edu

Funding information
National Science Foundation, Grant/Award Numbers: 1720212, 1818783, 2012490

Abstract

The anisotropic phase-field dendritic crystal growth model is a highly nonlinear system that couples the anisotropic Allen–Cahn equation and the thermal equation together. Due to the high anisotropy and nonlinear couplings in the system, how to develop an accurate and efficient, especially a fully decoupled scheme, has always been a challenging problem. To solve the challenge, in this article, we construct a novel fully decoupled numerical scheme which is also linear, energy stable, and second-order time accurate. The key idea to realize the full decoupling structure is to introduce an ordinary differential equation to deal with the nonlinear coupling terms satisfying the so-called "zero-energy-contribution" property. This scheme is very effective and easy to implement since only a few fully decoupled elliptic equations with constant coefficients need to be solved at each time step. We rigorously prove the solvability of each step and the unconditional energy stability, and perform a large number of numerical simulations in 2D and 3D to demonstrate its stability and accuracy numerically.

KEYWORDS

Allen–Cahn, dendritic, fully decoupled, phase-field, second-order, unconditional energy stability

1 | INTRODUCTION

Many crystals, especially metal crystals, exhibit dendritic growth when the following two conditions are met: (i) the mother liquid in the periphery of the crystal has an appropriate supercooled or negative temperature gradient component; and (ii) the crystal has a specific orientation concerning its growth interface. In daily life, dendritic crystals are very common, such as snowflakes/frost patterns, metal solidification, or crystals formed in supersaturated solutions due to changes in external conditions, and so on. For the mathematical modeling and numerical simulation of the dynamic process of dendrites, the phase-field method has been widely used in this topic due to its simple and flexible characteristics. Mathematically, the governing equations of the phase-field model are obtained by using the gradient flow method, that is, the postulated total free energy is minimized in a specific space. For the general phase-field dendritic crystal growth model, the total free energy consists of three parts, the conformational entropy specifying the spatial anisotropy, the double-well nonlinear potential achieving the separation of liquid and solid phases, as well as the thermal energy. Formally, if the melt convection in the liquid phase is neglected, the simplest governing system consists of two equations, including the

Allen–Cahn equation that controls the anisotropy of the crystal, and the heat equation that defines that the latent heat transfer must pass through the liquid-solid interface.

The focus of this article is to develop an effective numerical scheme for solving the phase-field dendritic crystal growth model proposed in References 1,2. As we all know, the core problem of the numerical algorithm development of the stiff phase-field model is how to design appropriate time discretization for the nonlinear terms, so that the resulting numerical scheme can maintain energy stability unconditionally. It is worth noting that the phase-field dendritic crystal growth model has been concerned for about two decades and a large number of modeling/numerical studies had been focused on it (see References 1-14). For such a highly complex nonlinear system, however, it is still very difficult to develop an easy-to-use and unconditionally stable numerical scheme because the model contains a lot of difficult nonlinearities and coupling terms, such as (i) the anisotropic coefficient (which may cause large oscillations), (ii) nonlinear double-well potential, and (iii) nonlinear coupling between phase-field variable and temperature. Especially for the difficulty (iii), at present, it is unclear how to achieve second-order time accuracy and full decoupling while possessing the unconditional energy stability at the same time. As far as the author knows, the only energy-stable and second-order time marching scheme was developed in Reference 15, in which the invariant energy quadratization (IEQ) method is used to discretize the nonlinear potential. However, the scheme is fully coupled, and at each time step, an elliptic system with variable coefficients needs to be solved which needs relatively high computational cost. The only fully decoupled and unconditionally energy stable scheme was developed in References 16,17, in which the main idea is to add a first-order stabilization term to the explicit processing of latent heat term (see the details in Remark 9). This explicit stabilization technique can decouple the calculation of the heat equation and the phase-field equation and plays a key role in establishing energy stability. However, its disadvantage is that it only has first-order accuracy in time, and it seems very challenging to upgrade it to a second-order version.

Therefore, the focus of this article is to construct a novel fully decoupled scheme for the phase-field dendritic growth model which not only has second-order accuracy but also decouples the calculation of the each variable at each time step. Meanwhile, we also expect the scheme to be linear and unconditionally energy stable. To this end, we note that the two coupled terms related to the latent heat satisfy a so-called "zero-energy-contribution" feature. That is, when deducing the energy law, after applying the inner products of some appropriate functions, the results of these two terms will completely cancel out. Thus, using this property, we introduce a nonlocal variable and design an ordinary differential equation (ODE) related to it that contains the inner products of these terms with some specific functions. This ODE is trivial at the continuous level because all the terms contained in it are zero. But after discretization, it can help eliminate all the troublesome nonlinear terms that are explicitly processed, thereby obtaining the unconditional energy stability. Besides, the introduction of the new nonlocal variable play a key role to decompose each discrete equation into multiple subequations that can be solved independently, thereby obtaining the fully decoupled structure.

By combining this novel decoupling method with the existing proven effective methods (scalar auxiliary variable [SAV] method that linearizes the nonlinear energy potential, see References 18,19), we finally arrive at an effective numerical scheme which is highly efficient in practice. At each time step we only need to solve several fully decoupled linear elliptic equations with constant coefficients. We further prove the solvability of each step and unconditional energy stability of the scheme strictly and carry out a large number of numerical simulations in 2D and 3D. The decoupling technique developed in this article can be also used to construct efficient decoupled type schemes for many coupled nonlinear models, not only the heat equation discussed in this article but also the other coupling type models, for example, the hydrodynamics-coupled model[20,21] and the magnetic field or electric field-coupled models.[22-24]

The rest of the article is organized as follows. In Section 2, we briefly describe the phase-field dendritic growth model and derive its energy structure. In Section 3, we construct the fully decoupled numerical scheme and describe its implementations in detail. The unconditional energy stability and solvability are proved rigorously as well. In Section 4, we implement the developed scheme and test its accuracy/stability by simulating a large number of fourfold/sixfold anisotropic crystal growth examples in 2D and 3D. Some concluding observations are in Section 5.

2 | THE ANISOTROPIC DENDRITIC PHASE-FIELD MODEL

Now, we briefly introduce the phase-field model describing the dynamical growth of the dendrites proposed in References 1,2. Suppose $\Omega \in \mathbb{R}^d$ with $d = 2, 3$ is a smooth, open, bounded, connected domain. We introduce a scalar function $\phi(\boldsymbol{x}, t)$, which is an order parameter used to label the liquid and solid phases, that is,

$$\phi(\boldsymbol{x}, t) = \begin{cases} 1 & \text{solid,} \\ -1 & \text{liquid,} \end{cases} \tag{1}$$

with a thin, smooth transition region with a width $O(\epsilon)$. The postulated total free energy describing the growth of anisotropic dendrites read as follows:

$$E(\phi, T) = \int_\Omega \left(\frac{1}{2} |\kappa(\nabla\phi)\nabla\phi|^2 + \frac{1}{4\epsilon^2} F(\phi) + \frac{\lambda}{2\epsilon K} T^2 \right) d\boldsymbol{x}, \tag{2}$$

where $T(\boldsymbol{x}, t)$ is the dimensionless temperature field, λ, K are positive parameters, and K is called as the "latent heat" parameter (which is named in Reference 4), $F(\phi) = (\phi^2 - 1)^2$ is a double-well type Ginzburg–Landau potential, $\kappa(\nabla\phi)$ is the anisotropic coefficient that is usually given by

$$\kappa(\nabla\phi) = 1 + \epsilon_4 \cos(m\Theta), \tag{3}$$

where m is the number of folds of anisotropy, ϵ_4 is an anisotropic strength parameter, $\Theta = \arctan(\frac{\phi_y}{\phi_x})$. When $m = 4$ (fourfold anisotropy), $\kappa(\nabla\phi)$ can be set as the function of the variable ϕ (cf. References 2,25), that is, for 2D,

$$\kappa(\nabla\phi) = (1 - 3\epsilon_4) \left(1 + \frac{4\epsilon_4}{1 - 3\epsilon_4} \frac{\phi_x^4 + \phi_y^4}{|\nabla\phi|^4} \right); \tag{4}$$

and for 3D,

$$\kappa(\nabla\phi) = (1 - 3\epsilon_4) \left(1 + \frac{4\epsilon_4}{1 - 3\epsilon_4} \frac{\phi_x^4 + \phi_y^4 + \phi_z^4}{|\nabla\phi|^4} \right). \tag{5}$$

By adopting the so-called variational form (VF) method given in Reference 2, the governing equations for ϕ and T reads as:

$$\tau\phi_t = -\frac{\delta E}{\delta\phi} - \frac{\lambda}{\epsilon} p(\phi) T,$$

$$= \nabla \cdot (\kappa^2(\nabla\phi)\nabla\phi + \kappa(\nabla\phi)|\nabla\phi|^2 \zeta(\phi)) - \frac{1}{\epsilon^2} f(\phi) - \frac{\lambda}{\epsilon} p(\phi) T, \tag{6}$$

$$T_t = D\Delta T + K p(\phi) \phi_t. \tag{7}$$

Remark 1. The VF method that had been used to derive the partial differential equation (PDE) system (6)–(7) can be regarded as the mixed variational approach of the L^2 gradient flow approach (or called Allen–Cahn dynamics) that is used to derive the equation for ϕ, and the H^{-1} gradient flow approach (or called Cahn–Hilliard dynamics) that is used for the dimensionless enthalpy $T - \frac{G(\phi)}{2}$ with $G'(\phi) = p(\phi)$, which in turn gives the equation for T. The details can be found in page 4323 of Reference 2, equation (11)–(12)–(15) and the choices of functional given in (23)–(24). The model parameters in (6)–(7) is simply the rescaling of model parameters used in Reference 2.

We explain the notations in (6)–(7). $\frac{\delta E}{\delta\phi}$ is the variational derivative of the total free energy related to ϕ, $\tau > 0$ is the mobility constant, D is the temperature diffusion rate, $p(\phi) = (1 - \phi^2)^2$ indicates that latent heat is transferred only through the liquid–solid interface,[26] $\zeta(\phi)$ is the variational derivative of $\kappa(\nabla\phi)$. In 2D, $\zeta(\phi)$ reads as

$$\zeta(\phi) = \frac{\delta\kappa(\nabla\phi)}{\delta\phi} = 4\epsilon_4 \frac{4}{|\nabla\phi|^6} \left(\phi_x(\phi_x^2\phi_y^2 - \phi_y^4), \ \phi_y(\phi_x^2\phi_y^2 - \phi_x^4) \right), \tag{8}$$

and in 3D, $\zeta(\phi)$ reads as

$$\zeta(\phi) = \frac{\delta\kappa(\nabla\phi)}{\delta\phi} = 4\epsilon_4 \frac{4}{|\nabla\phi|^6} \left(\phi_x(\phi_x^2\phi_y^2 + \phi_x^2\phi_z^2 - \phi_y^4 - \phi_z^4), \right.$$

$$\left. \phi_y(\phi_y^2\phi_z^2 + \phi_x^2\phi_y^2 - \phi_x^4 - \phi_z^4), \ \phi_z(\phi_x^2\phi_z^2 + \phi_y^2\phi_z^2 - \phi_x^4 - \phi_y^4) \right). \tag{9}$$

Regarding the boundary conditions, in order to eliminate all the complexity associated with boundary integrals, in this study, we use periodic boundary conditions or flux-free homogenous Neumann boundary conditions, or a combination thereof:

$$\text{(i) } \phi \text{ and } T \text{ are periodic; or (ii) } \partial_{\mathbf{n}}\phi|_{\partial\Omega} = \partial_{\mathbf{n}}T|_{\partial\Omega} = 0, \tag{10}$$

where n is the outward normal of the computational domain Ω. The initial conditions of the system read as

$$\phi|_{(t=0)} = \phi^0, T|_{(t=0)} = T^0. \tag{11}$$

The phase-field dendritic system (6)–(7) admits the law of energy dissipation which can be derived by the following process. Before introducing it, some notations are given here. The L^2 inner product of any two functions $\phi(\mathbf{x})$ and $\psi(\mathbf{x})$ is denoted by $(\phi(\mathbf{x}), \psi(\mathbf{x})) = \int_\Omega \phi(\mathbf{x})\psi(\mathbf{x})d\mathbf{x}$, and the L^2 norm of $\phi(\mathbf{x})$ is denoted by $\|\phi\|^2 = (\phi, \phi)$. To get the energy law of the system, first, by multiplying the inner product of (6) with ϕ_t in L^2 and using the integration by parts, we derive

$$\tau\|\phi_t\|^2 + \frac{d}{dt}\int_\Omega \left(\frac{1}{2}|\kappa(\nabla\phi)\nabla\phi|^2 + \frac{1}{4\epsilon^2}F(\phi)\right)d\mathbf{x} = \underbrace{-\frac{\lambda}{\epsilon}(p(\phi)T, \phi_t)}_{I}. \tag{12}$$

By taking the L^2 inner product of (7) with $\frac{\lambda}{\epsilon K}T$ and using the integration by parts, we obtain

$$\frac{d}{dt}\int_\Omega \frac{\lambda}{2\epsilon K}T^2 d\mathbf{x} + \frac{D\lambda}{\epsilon K}\|\nabla T\|^2 = \underbrace{\frac{\lambda}{\epsilon}(p(\phi)\phi_t, T)}_{II}. \tag{13}$$

Combining the two obtained equalities and noting that the terms I and II are canceled, we get

$$\frac{d}{dt}E(\phi, T) = -\tau\|\phi_t\|^2 - \frac{\lambda D}{\epsilon K}\|\nabla T\|^2 \leq 0, \tag{14}$$

where the combination of the two negative terms specifies the diffusion rate of the total free energy.

Remark 2. When deriving the PDE energy law (14), we notice that the terms I and II cancel each other out, which indicates that they do not make any contribution to the total free energy or energy diffusion rate. Thus they can be called to satisfy a "zero-energy-contribution" feature. This "zero-energy-contribution" feature behind these terms provides some guidance for the development of the decoupling type schemes, which will be given in the next section.

3 | NUMERICAL SCHEME

We aim to construct a time marching scheme to solve the system (6)–(7). For those terms that cause great difficulties, including the cubic polynomial $f(\phi)$, the anisotropic gradient entropy related to $\kappa(\nabla\phi)$, and the two coupled terms related to $p(\phi)$, we need develop special techniques to discretize them according to the needs. For example, if we only need to discretize $f(\phi)$, then there exist many successful methods to deal with it, including nonlinear methods (convex-splitting, etc.) and linear methods (linear stabilization, IEQ, SAV, etc.), see References 27-38. If a scheme with linearity, second-order temporal accuracy, and unconditional energy stability is needed, we can use the second-order IEQ method, as shown in Reference 15. But that method cannot achieve the full decoupling. If a scheme with full decoupling, linearity, and unconditional energy stability is needed, we can use the first-order IEQ method and add a linear stabilizer to the explicit processing of the latent heat, as shown in Reference 16. But that method cannot achieve the temporal second-order accuracy. If we need all these characteristics, that is to say, we expect a scheme that can achieve full decoupling, linearity, second-order temporal accuracy, and maintain unconditional energy stability, then as far as the author knows, it is not clear whether this method exists.

Therefore, in this article, we expect to construct the first time marching scheme that achieves the desired properties of second-order accuracy in time, full decoupling, linearity, and unconditional energy stability. As can be seen from the

above-summarized description for available approaches, the main difficulties are concentrated on how to develop efficient discretization methods for coupled nonlinear terms associated with $p(\phi)$. Utilizing the "zero-energy-contribution" feature that they satisfy, we design a novel method to deal with them and combine it with the existing methods (the SAV method to linearize the energy potential) to obtain an effective scheme. The detailed process is given as follows.

3.1 | Reformulation

First, we introduce a nonlocal scalar auxiliary variable $Q(t)$ and design a special time evolution ODE for it, that reads as

$$
\begin{cases}
Q_t = \int_\Omega (p(\phi)T\phi_t - p(\phi)\phi_t T)d\boldsymbol{x}, \\
Q|_{(t=0)} = 1.
\end{cases}
\tag{15}
$$

It is easy to see that $Q_t = 0$, $Q|_{(t=0)} = 1$ which means $Q(t)$ only has a trivial solution of $Q(t) = 1$. Now we combine this trivial ODE (15) with the original PDE system (6)–(7) to form the following equivalent system

$$
\tau\phi_t = \nabla \cdot (\kappa^2(\nabla\phi)\nabla\phi + \kappa(\nabla\phi)|\nabla\phi|^2\boldsymbol{\zeta}(\phi)) - \frac{1}{\epsilon^2}f(\phi) - \frac{\lambda}{\epsilon}\underbrace{Qp(\phi)T}_{\text{modification by Q}},
\tag{16}
$$

$$
T_t = D\Delta T + K\underbrace{Qp(\phi)\phi_t}_{\text{modification by Q}},
\tag{17}
$$

$$
Q_t = \int_\Omega (p(\phi)T\phi_t - p(\phi)\phi_t T)d\boldsymbol{x}, \quad Q|_{(t=0)} = 1.
\tag{18}
$$

Remark 3. We must notice there are two modifications that have been made to the original system (6)–(7) to obtain the new system (16)–(18). The modification is that we multiply the latent heat terms in (21) and (23) with Q. This modification is trivial since $Q(t) = 1$ from (18). Therefore, the new system (16)–(18) using the variables (ϕ, T, Q) is equivalent to the original PDE system (6)–(7) using the variables (ϕ, T).

Second, we define a nonlocal scalar auxiliary variable $U(t)$ to quadratize the energy potential as

$$
U(t) = \sqrt{\int_\Omega \left(\frac{1}{2}(\kappa^2(\nabla\phi) - C_1)|\nabla\phi|^2 + \frac{1}{4\epsilon^2}(F(\phi) - 2C_2\phi^2) \right) d\boldsymbol{x} + B},
\tag{19}
$$

where C_1 $(0 < C_1 < (1 - \epsilon_4)^2)$ and C_2 are two preallocated positive constants. Note that $F(\phi)$ is a quartic polynomial, so it can always bound the C_2 term from below. Moreover, $\kappa^2(\nabla\phi) \geq (1 - \epsilon_4)^2$, so the integral term in (19) can be guaranteed to be bounded from below. The constant B is added to make the radians further positive. This auxiliary nonlocal function U helps to transfer nonlinear part of the total free energy (as long as it is bounded from below) into a quadratic form, that is, the new total free energy reads as

$$
E(\phi, T, U) = \int_\Omega \left(\frac{C_1}{2}|\nabla\phi|^2 + \frac{C_2}{2\epsilon^2}|\phi|^2 + \frac{\lambda}{2\epsilon K}T^2 \right) d\boldsymbol{x} + U^2 - B.
\tag{20}
$$

It can be seen that the two terms related to C_i in the new energy formula (20) can be used to ensure the H^1-stability of ϕ.

Then, we continue to rewrite the dendritic system (16)–(18) to the following equivalent form:

$$
\tau\phi_t - C_1\Delta\phi + \frac{C_2}{\epsilon^2}\phi = -HU - \frac{\lambda}{\epsilon}Qp(\phi)T,
\tag{21}
$$

$$
U_t = \frac{1}{2}\int_\Omega H\phi_t d\boldsymbol{x},
\tag{22}
$$

$$
T_t = D\Delta T + KQp(\phi)\phi_t,
\tag{23}
$$

$$
Q_t = \int_\Omega (p(\phi)T\phi_t - p(\phi)\phi_t T)d\boldsymbol{x},
\tag{24}
$$

where

$$H(\phi) = \frac{-\nabla \cdot (\kappa^2(\nabla\phi)\nabla\phi + \kappa(\nabla\phi)|\nabla\phi|^2\zeta(\phi)) + \frac{1}{\epsilon^2}f(\phi)}{\sqrt{\int_\Omega \left(\frac{1}{2}|\kappa(\nabla\phi)\nabla\phi|^2 + \frac{1}{4\epsilon^2}F(\phi)\right)d\boldsymbol{x} + B}}. \tag{25}$$

The initial conditions read as

$$\begin{cases} \phi|_{(t=0)} = \phi^0, \\ T|_{(t=0)} = T^0, \\ Q|_{(t=0)} = 1, \\ U|_{(t=0)} = \sqrt{\int_\Omega \left(\frac{1}{2}(\kappa^2(\nabla\phi^0) - C_1)|\nabla\phi^0|^2 + \frac{1}{4\epsilon^2}(F(\phi^0) - 2C_2\phi^{0^2})\right)d\boldsymbol{x} + B}. \end{cases} \tag{26}$$

The boundary conditions of the new system (21)–(24) are still (10).

Remark 4. We explain the further modification that have been made to the system (16)–(18) to obtain the new system (21)–(24), in which (16) is reformulated by using the new variables U, and the time derivative of U is performed to obtain (22). These two systems are also equivalent and we can easily restore the (21)–(24) back to (16)–(18) by integrating (22) with the initial conditions given in (26) for $U|_{(t=0)}$. Therefore, we highlight the three PDE systems (6)–(7), (16)–(18), (21)–(24) are all equivalent.

We highlight a basic strategy that has been widely adopted in algorithm development. If it is challenging to develop an algorithm for the original system, then one commonly used strategy is to use some techniques to rewrite it into an equivalent system, which may be more convenient for algorithm developments. This simple and effective strategy has been adopted in the algorithm design of many complicated models. For example, for stability reasons, the advective terms in Navier–Stokes equation with variable density is reformulated (cf. Reference 39); to avoid solving the pressure Poisson equation with variable coefficients, the penalty method reformulates the divergence-free condition of the velocity field for the Navier–Stokes equation (cf. References 40-42); for the reasons of obtaining linear schemes, the IEQ/SAV methods reformulates the energy potentials to quadratic form (cf. References 15,18,19,43). Based on this basic logic, we rewrite the original PDE system twice to form the equivalent system, which is relatively convenient to design numerical schemes with desired properties including linear, second-order accurate, fully decoupled, unconditional energy stable.

The transformed system (21)–(24) is an energy dissipative system as well. Its energy dissipative law can be obtained by performing a similar process to obtain (14). We present the details here since the discrete energy stability proof follows the same line. By taking the L^2 inner product of (21) with ϕ_t, we derive

$$\tau\|\phi_t\|^2 + \frac{d}{dt}\left(\frac{C_1}{2}\|\nabla\phi\|^2 + \frac{C_2}{2\epsilon^2}\|\phi\|^2\right) = -U\int_\Omega H\phi_t d\boldsymbol{x} - \underbrace{\frac{\lambda}{\epsilon}Q\int_\Omega p(\phi)T\phi_t d\boldsymbol{x}}_{I_1}. \tag{27}$$

By multiplying of (22) with $2U$, we obtain

$$\frac{d}{dt}|U|^2 = U\int_\Omega H\phi_t d\boldsymbol{x}. \tag{28}$$

We take the L^2 inner product of (23) with $\frac{\lambda}{\epsilon K}T$ to obtain

$$\frac{d}{dt}\left(\frac{\lambda}{2\epsilon K}\|T\|^2\right) = -\frac{D\lambda}{\epsilon K}\|\nabla T\|^2 + \underbrace{\frac{\lambda}{\epsilon}Q\int_\Omega p(\phi)\phi_t T d\boldsymbol{x}}_{II_1}. \tag{29}$$

By multiplying of (24) with $\frac{\lambda}{\epsilon}Q$, we obtain

$$\frac{d}{dt}\left(\frac{\lambda}{2\epsilon}|Q|^2\right) = \underbrace{\frac{\lambda}{\epsilon}Q\int_\Omega p(\phi)T\phi_t d\boldsymbol{x}}_{I_2} - \underbrace{\frac{\lambda}{\epsilon}Q\int_\Omega p(\phi)\phi_t T d\boldsymbol{x}}_{II_2}. \tag{30}$$

By combining the above four equalities, we obtain the energy law as follows,

$$\frac{d}{dt}\left(\frac{C_1}{2}\|\nabla\phi\|^2 + \frac{C_2}{2\epsilon^2}\|\phi\|^2 + \frac{\lambda}{2\epsilon K}\|T\|^2 + |U|^2 + \frac{\lambda}{2\epsilon}|Q|^2\right) = -\tau\|\phi_t\|^2 - \frac{D\lambda}{\epsilon K}\|\nabla T\|^2 \leq 0. \tag{31}$$

Remark 5. The advantage of adding a trivial differential equation for Q to the system can be seen from the process deriving the energy law (31). That is, the two nonlinear integrals in category I (I_1 and I_2) and category II (II_1 and II_2) will be canceled separately. We do not need to use the term I_1 to offset the term II_1 as deriving (14). This approach brings a great benefit when designing decoupled schemes because terms I_1 and II_1 will be discretized in different ways such that they can no longer cancel each other out. At this time, the nonlinear terms in (24) will play a role in countering them, which makes it possible to design a fully decoupled scheme.

3.2 | Second-order fully decoupled scheme

We denote $\delta t > 0$ as a time step size and $t^n = n\delta t$ for $0 \leq n \leq N$ with $T = N\delta t$. Let ψ^n be the numerical approximation to the analytic function $\psi(\cdot, t)|_{t=t^n}$.

Now, we are ready to develop a numerical scheme based on the second-order backward differentiation formula to discretize the new system (21)–(24), which reads as follows.

Given $(\phi, T, U, Q)^n$ and $(\phi, T, U, Q)^{n-1}$, we compute $(\phi, T, U, Q)^{n+1}$ by the following scheme:

$$\tau\frac{a\phi^{n+1} - b\phi^n + c\phi^{n-1}}{2\delta t} - C_1\Delta\phi^{n+1} + \frac{C_2}{\epsilon^2}\phi^{n+1} = -H^*U^{n+1} - \frac{\lambda}{\epsilon}Q^{n+1}p(\phi^*)T^*, \tag{32}$$

$$aU^{n+1} - bU^n + cU^{n-1} = \frac{1}{2}\int_\Omega H^*(a\phi^{n+1} - b\phi^n + c\phi^{n-1})d\mathbf{x}, \tag{33}$$

$$\frac{aT^{n+1} - bT^n + cT^{n-1}}{2\delta t} = D\Delta T^{n+1} + KQ^{n+1}p(\phi^*)\phi_t^*, \tag{34}$$

$$\frac{aQ^{n+1} - bQ^n + cQ^{n-1}}{2\delta t} = \int_\Omega\left(p(\phi^*)T^*\frac{a\phi^{n+1} - b\phi^n + c\phi^{n-1}}{2\delta t} - p(\phi^*)\phi_t^*T^{n+1}\right)d\mathbf{x}, \tag{35}$$

where

$$a = 3, b = 4, c = 1,$$
$$\phi^* = 2\phi^n - \phi^{n-1}, T^* = 2T^n - T^{n-1},$$
$$H^* = H(\phi^*),$$
$$\phi_t^* = \frac{5\phi^n - 8\phi^{n-1} + 3\phi^{n-2}}{2\delta t}, \tag{36}$$

$C_i, i = 1, 2$, are two positive stabilization parameters with $0 < C_1 < (1 - \epsilon)^2$ (see the definition of $U(t)$ in (19)). The boundary conditions are either periodic or

$$\partial_n\phi^{n+1}|_{\partial\Omega} = \partial_n T^{n+1}|_{\partial\Omega} = 0. \tag{37}$$

We give detailed explanations of the above scheme in the following remarks.

Remark 6. The startup computation of the scheme (32)–(35) requires the values of all variables at $t = t^1, t^2$. In practice, we obtain these values by constructing a first-order scheme based on the backward Euler method which can easily obtained by setting $a = b = 2, c = 0, \psi^* = \psi^n$ for all variables ψ, and $\phi_t^* = \frac{\phi^{n+1}-\phi^n}{\delta t}$. We notice that the first-order scheme is a coupled scheme for ϕ and T, so it requires relatively more computational cost. But since we only need to calculate the first two steps at $t = t^1, t^2$, these computational costs can be ignored.

Remark 7. Due to the discretization method used in (35), it is easy to see that Q^{n+1} is no longer equal to $Q(t)|_{t=t^{n+1}}$ (i.e., 1), because the nonlinear terms contained in (35) no longer strictly equals to zero. For the benefit of the reader, we explain here why we allow this to happen as follows.

As we all know, the purpose of constructing a numerical algorithm is to establish the approximation value of the exact solution of the PDE system with a certain order of accuracy. In last subsection, we give sufficient descriptions to show that the reformulated system (21)–(24) is equivalent to the original system (6)–(7). Therefore, if the developed numerical algorithm does approximate the PDE system with a certain time accuracy, all variables involved in the calculation should also correspond to that approximation order of accuracy. This means that we have no reason to impose excessive and unreasonable request of expecting that Q^{n+1} must be strictly equal to $Q(t)|_{t=t^{n+1}}$, since Q^{n+1} is also a second-order approximation to $Q(t)|_{t=t^{n+1}}$. This is similar to that ϕ^{n+1} is just a second-order approximation to $\phi(t)|_{t=t^{n+1}}$, and all unknown variables including $Q^{n+1}, U^{n+1}, \phi^{n+1}, T^{n+1}$ in the scheme (32)–(35) are just second-order approximations to $(Q(t), U(t), \phi(t), T(t))|_{t=t^{n+1}}$ in the PDE system (21)–(24).

Remark 8. The two stabilization terms related to $C_i, i = 1, 2$ in are two key terms to ensure the H^1 stability of the reformulated PDE system (21)–(24) and the developed numerical scheme. Note that the coefficient H^* contains almost all explicitly processed terms, including the second-order term. As we all know, the explicit processing method used for higher-order linear terms is unstable, so we have to restore the higher-order terms by using the stabilizer, which is the reason for adding the C_1 term. The use of C_2 term is for similar reason and it is used to balance the explicit processed terms $f(\phi)$ contained in H^*. In Section 4, we provide numerical evidence to show that these stabilizers are important for enhancing the energy stability of the numerical schemes while using larger time steps, see Figures 1 and 2.

Moreover, for models are either with very high stiffness issue due to the model parameters, or with very strong anisotropy so that spatial oscillations can induce severe constraints on the time step, while the SAV (or IEQ) methods applied to these models are formally unconditionally energy stable, but exceedingly small time steps are needed to achieve reasonable accuracy. To fix such an inherent deficiency, we simply need to combine SAV/IEQ approaches with the stabilization technique to construct stabilized-SAV (S-IEQ) methods. More precisely, by adding one or several suitable linear stabilization terms and treating involved nonlinear terms in the semiexplicit way, we can construct unconditionally energy stable schemes which are easily solvable and can produce accurate results with reasonable time steps. We refer to a recent review paper in Reference 18 for various linear stabilization terms for a series of models with high stiffness.

3.3 | Implementation

Formally, the developed scheme (32)–(35) exhibits a fully coupled nature because all variables are closely related through the variable Q, although it is linear and consistent with the second-order accuracy of time. To achieve the complete decoupling, we take advantage of the special feature of this scheme, that is, there is no need to explicitly solve the two auxiliary variables U and Q. Instead, these auxiliary variables can help to simplify all equations so that they can be solved separately. The specific implementation process is described as follows.
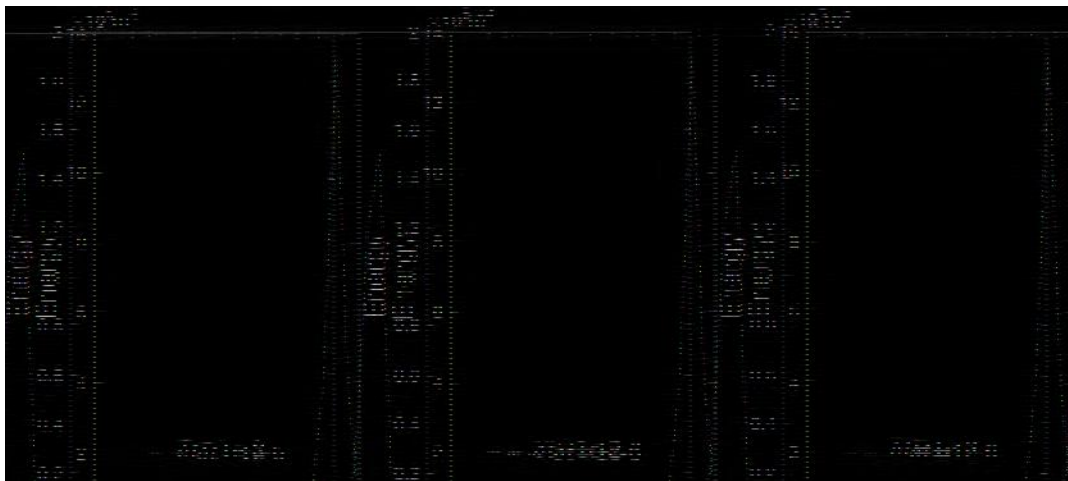

FIGURE 1 Stability tests using the stabilization parameter set (I), where the total free energy (61) computed by using two different time steps (A) $\delta t = 1e - 2$ and (B) $\delta t = 1e - 6$ is plotted
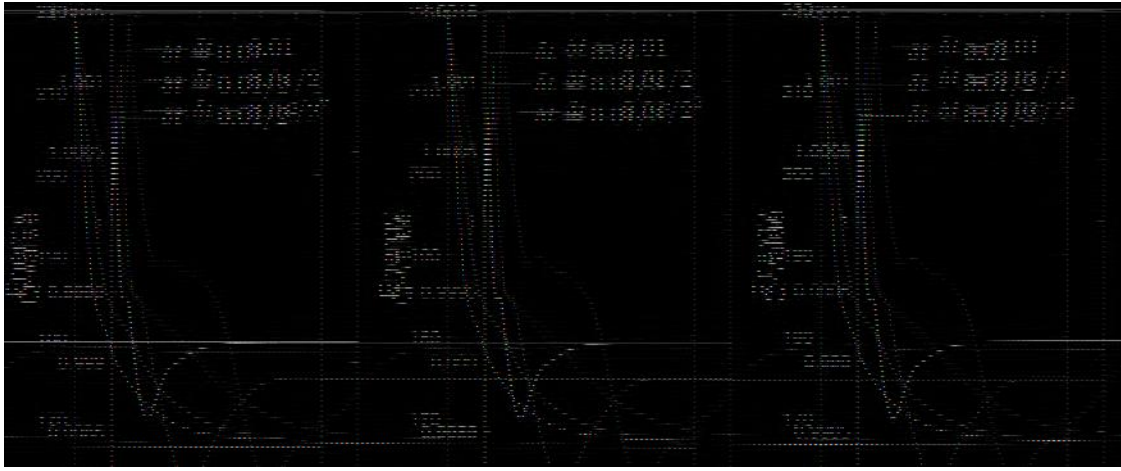
FIGURE 2 (A) Stability tests using the stabilization parameter set (II), where the curves plot the time evolutions of the total free energy (61) computed using different time steps; (B) the time evolution of the second auxiliary variable Q computed using various time steps

First, we use the nonlocal variable Q^{n+1} to split $(\phi, T, U)^{n+1}$ into a linear combination form that reads as

$$
\begin{cases}
\phi^{n+1} = \phi_1^{n+1} + Q^{n+1}\phi_2^{n+1}, \\
T^{n+1} = T_1^{n+1} + Q^{n+1}T_2^{n+1}, \\
U^{n+1} = U_1^{n+1} + Q^{n+1}U_2^{n+1}.
\end{cases}
\tag{38}
$$

Then the scheme (32) and (34) can be rewritten as

$$
\begin{cases}
\tau \frac{a(\phi_1^{n+1} + Q^{n+1}\phi_2^{n+1}) - b\phi^n + c\phi^{n-1}}{2\delta t} - C_1 \Delta(\phi_1^{n+1} + Q^{n+1}\phi_2^{n+1}) \\
+ \frac{C_2}{\epsilon^2}(\phi_1^{n+1} + Q^{n+1}\phi_2^{n+1}) \\
= -H^*(U_1^{n+1} + Q^{n+1}U_2^{n+1}) - \frac{\lambda}{\epsilon} Q^{n+1} p(\phi^*)T^*, \\
\frac{a(T_1^{n+1} + Q^{n+1}T_2^{n+1}) - bT^n + cT^{n-1}}{2\delta t} = D\Delta(T_1^{n+1} + Q^{n+1}T_2^{n+1}) + KQ^{n+1}p(\phi^*)\phi_t^*.
\end{cases}
\tag{39}
$$

According to Q^{n+1}, each equation in the above can be split into two subequations as

$$
\begin{cases}
\tau \frac{a\phi_1^{n+1}}{\delta t} - C_1 \Delta\phi_1^{n+1} + \frac{C_2}{\epsilon^2}\phi_1^{n+1} + H^*U_1^{n+1} = \tau \frac{b\phi^n - c\phi^{n-1}}{2\delta t}, \\
\tau \frac{a\phi_2^{n+1}}{\delta t} - C_1 \Delta\phi_2^{n+1} + \frac{C_2}{\epsilon^2}\phi_2^{n+1} + H^*U_2^{n+1} = -\frac{\lambda}{\epsilon}p(\phi^*)T^*,
\end{cases}
\tag{40}
$$

and

$$
\begin{cases}
\frac{aT_1^{n+1}}{2\delta t} - D\Delta T_1^{n+1} = \frac{bT^n - cT^{n-1}}{2\delta t}, \\
\frac{aT_2^{n+1}}{2\delta t} - D\Delta T_2^{n+1} = Kp(\phi^*)\phi_t^*.
\end{cases}
\tag{41}
$$

The boundary conditions of the above four equations are either periodic or

$$
\partial_n(\phi_1, \phi_2, T_1, T_2)^{n+1}|_{\partial\Omega} = 0.
\tag{42}
$$

Meanwhile, note the two equations in (41) are linear elliptic equations and all terms on the right end are explicit, thus $(T_1, T_2)^{n+1}$ can be solved easily.

Second, using the nonlocal variables U_1^{n+1} and U_2^{n+1}, we split the variables $(\phi_1, \phi_2)^{n+1}$ as the following form

$$
\begin{cases}
\phi_1^{n+1} = \phi_{11}^{n+1} + U_1^{n+1}\phi_{12}^{n+1}, \\
\phi_2^{n+1} = \phi_{21}^{n+1} + U_2^{n+1}\phi_{22}^{n+1}.
\end{cases}
\tag{43}
$$

Replacing $(\phi_1, \phi_2)^{n+1}$ in (40) using (43), and splitting the obtained equations according to U_1^{n+1} and U_2^{n+1}, we get the following four subequations,

$$
\begin{cases}
\tau\frac{a\phi_{11}^{n+1}}{\delta t} - C_1\Delta\phi_{11}^{n+1} + \frac{C_2}{\epsilon^2}\phi_{11}^{n+1} = G_1, \\
\tau\frac{a\phi_{12}^{n+1}}{\delta t} - C_1\Delta\phi_{12}^{n+1} + \frac{C_2}{\epsilon^2}\phi_{12}^{n+1} = G_2, \\
\tau\frac{a\phi_{21}^{n+1}}{\delta t} - C_1\Delta\phi_{21}^{n+1} + \frac{C_2}{\epsilon^2}\phi_{21}^{n+1} = G_3, \\
\tau\frac{a\phi_{22}^{n+1}}{\delta t} - C_1\Delta\phi_{22}^{n+1} + \frac{C_2}{\epsilon^2}\phi_{22}^{n+1} = G_4,
\end{cases}
\tag{44}
$$

where

$$
\begin{cases}
G_1 = \tau\frac{b\phi^n - c\phi^{n-1}}{2\delta t}, \\
G_2 = G_4 = -H^*, \\
G_3 = -\frac{\lambda}{\epsilon}p(\phi^*)T^*.
\end{cases}
\tag{45}
$$

The boundary conditions of the above four equations in (44) are either periodic or

$$
\partial_n(\phi_{11}, \phi_{12}, \phi_{21}, \phi_{22})^{n+1}|_{\partial\Omega} = 0.
\tag{46}
$$

Note $G_i, i = 1, 2, 3, 4$ are all explicit terms, and $G_2 = G_4$ means $\phi_{12}^{n+1} = \phi_{22}^{n+1}$. Hence we can easily solve three independent elliptic equations in (44) to get $(\phi_{11}, \phi_{12}, \phi_{21}, \phi_{22})^{n+1}$.

Third, we rewrite (33) as

$$
U^{n+1} = \frac{1}{2}\int_\Omega H^*\phi^{n+1}d\boldsymbol{x} + G_5,
\tag{47}
$$

where $G_5 = \frac{1}{a}(bU^n - cU^{n-1}) - \frac{1}{2a}\int_\Omega H^*(b\phi^n - c\phi^{n-1})d\boldsymbol{x}$. Replacing U^{n+1} and ϕ^{n+1} using the split form given in (38), we rewrite (47) as

$$
U_1^{n+1} + Q^{n+1}U_2^{n+1} = \frac{1}{2}\int_\Omega H^*(\phi_1^{n+1} + Q^{n+1}\phi_2^{n+1})d\boldsymbol{x} + G_5.
\tag{48}
$$

We split the above result according to Q^{n+1} to derive

$$
\begin{cases}
U_1^{n+1} = \frac{1}{2}\int_\Omega H^*\phi_1^{n+1}d\boldsymbol{x} + G_5, \\
U_2^{n+1} = \frac{1}{2}\int_\Omega H^*\phi_2^{n+1}d\boldsymbol{x}.
\end{cases}
\tag{49}
$$

We replace $(\phi_1, \phi_2)^{n+1}$ using the split form given in (43) to get

$$
\begin{cases}
U_1^{n+1} = \frac{1}{2}\int_\Omega H^*(\phi_{11}^{n+1} + U_1^{n+1}\phi_{12}^{n+1})d\boldsymbol{x} + G_5, \\
U_2^{n+1} = \frac{1}{2}\int_\Omega H^*(\phi_{21}^{n+1} + U_2^{n+1}\phi_{22}^{n+1})d\boldsymbol{x}.
\end{cases}
\tag{50}
$$

By applying the simple factorization for each equality in (50), we derive

$$
\begin{cases}
U_1^{n+1} = \dfrac{\frac{1}{2}\int_\Omega H^* \phi_{11}^{n+1} d\boldsymbol{x} + G^5}{1 - \frac{1}{2}\int_\Omega H^* \phi_{12}^{n+1} d\boldsymbol{x}}, \\[4mm]
U_2^{n+1} = \dfrac{\frac{1}{2}\int_\Omega H^* \phi_{21}^{n+1} d\boldsymbol{x}}{1 - \frac{1}{2}\int_\Omega H^* \phi_{22}^{n+1} d\boldsymbol{x}}.
\end{cases}
\tag{51}
$$

We need to verify (51) is solvable by showing the denominator $1 - \frac{1}{2}\int_\Omega H^* \phi_{22}^{n+1} d\boldsymbol{x} \neq 0$ (note $\phi_{12}^{n+1} = \phi_{22}^{n+1}$). By taking the L^2 inner product of the fourth equation in (44) with ϕ_{22}^{n+1}, and using integration by parts, we get

$$
-\int_\Omega H^* \phi_{22}^{n+1} d\boldsymbol{x} = \frac{\tau a}{\delta t}\|\phi_{22}^{n+1}\|^2 + C_1 \|\nabla\phi_{22}^{n+1}\|^2 + \frac{C_2}{\epsilon^2}\|\phi_{22}^{n+1}\|^2 \geq 0,
\tag{52}
$$

which implies (51) is solvable. After we get U_1^{n+1} and U_2^{n+1} from (51), we update $(\phi_1, \phi_2)^{n+1}$ from (43).

Fourth, we solve the auxiliary variable Q^{n+1}. Using the split form of the variables ϕ^{n+1} and T^{n+1} given in (38), one can rewrite (35) as the following form:

$$
\left(\frac{a}{2\delta t} - \eta_2\right) Q^{n+1} = \frac{1}{2\delta t}(bQ^n - cQ^{n-1}) + \eta_1,
\tag{53}
$$

where η_1, η_2 are two explicit terms which are given by

$$
\begin{cases}
\eta_1 = \int_\Omega p(\phi^*) T^* \dfrac{a\phi_1^{n+1} - b\phi^n + c\phi^{n-1}}{2\delta t} d\boldsymbol{x} - \int_\Omega p(\phi^*)\phi_t^* T_1^{n+1} d\boldsymbol{x}, \\[3mm]
\eta_2 = \int_\Omega p(\phi^*) T^* \dfrac{a\phi_2^{n+1}}{2\delta t} d\boldsymbol{x} - \int_\Omega p(\phi^*)\phi_t^* T_2^{n+1} d\boldsymbol{x}.
\end{cases}
\tag{54}
$$

We need to verify (53) is solvable by showing $\frac{a}{2\delta t} - \eta_2 \neq 0$. By taking the L^2 inner product of the second equation in (40) with ϕ_2^{n+1}, we obtain

$$
-\frac{\lambda}{\epsilon}\int_\Omega p(\phi^*) T^* \phi_2^{n+1} d\boldsymbol{x} = \tau\frac{a}{\delta t}\|\phi_2^{n+1}\|^2 + C_1\|\nabla\phi_2^{n+1}\|^2
$$
$$
+ \frac{C_2}{\epsilon^2}\|\phi_2^{n+1}\|^2 + U_2^{n+1}\int_\Omega H^* \phi_2^{n+1} d\boldsymbol{x}.
\tag{55}
$$

From the second equality in (49), it is easy to see that

$$
U_2^{n+1}\int_\Omega H^* \phi_2^{n+1} d\boldsymbol{x} = \frac{1}{2}\left(\int_\Omega H^* \phi_2^{n+1} d\boldsymbol{x}\right)^2,
\tag{56}
$$

which implies

$$
-\frac{\lambda}{\epsilon}\int_\Omega p(\phi^*) T^* \phi_2^{n+1} d\boldsymbol{x} \geq 0.
\tag{57}
$$

By taking the L^2 inner product of the second equation in (41) with T_2^{n+1}, we obtain

$$
K\int_\Omega p(\phi^*)\phi_t^* T_2^{n+1} d\boldsymbol{x} = \frac{a}{2\delta t}\|T_2^{n+1}\|^2 + D\|\nabla T_2^{n+1}\|^2 \geq 0.
\tag{58}
$$

From (57) and (58), we derive $-\eta_2 \geq 0$, which means that the unique solvability of (53) is then verified. Finally, we update $(\phi, T, U)^{n+1}$ from (38).

In short, the implementation of scheme (32)–(35) includes the following steps:

- *Step 1*: Compute $(T_1, T_2)^{n+1}$ from (41);

- *Step 2*: Compute $(\phi_{11}, \phi_{12}, \phi_{21}, \phi_{22})^{n+1}$ from (44);
- *Step 3*: Update $(U_1, U_2)^{n+1}$ from (51);
- *Step 4*: Update $(\phi_1, \phi_2)^{n+1}$ from (43);
- *Step 5*: Compute Q^{n+1} from (53);
- *Step 6*: Update $(\phi, T, U)^{n+1}$ from (38).

Therefore, in summary, the total cost of solving the scheme (32)–(35) at each time step includes solving two elliptic equations in Step 1, and three more elliptic equations in Step 2 (since $\phi_{12}^{n+1} = \phi_{22}^{n+1}$). All these equations have constant coefficients and are fully decoupled, which means the scheme can achieve very efficient calculations in practice.

Remark 9. For comparison, here we present another fully decoupled type energy-stable scheme constructed in References 16,17. Similar decoupling technique had also been used in various situations, see Reference 44,45. For simplicity, we only discretize the related terms while other terms remain continuously so that the readers can see more clearly. It reads as

$$
\begin{cases}
\dfrac{\phi^{n+1}-\phi^n}{\delta t} + \ldots\ldots = -\dfrac{\lambda}{\epsilon}p(\phi^n)(T^n + \underbrace{K\delta t p(\phi^n)\dfrac{\phi^{n+1}-\phi^n}{\delta t}}_{\text{stabilization term}}), \\[4mm]
\dfrac{T^{n+1}-T^n}{\delta t} + \ldots\ldots = \underbrace{Kp(\phi^n)\dfrac{\phi^{n+1}-\phi^n}{\delta t}}_{\text{explicit since }\phi^{n+1}\text{ is obtained above}}.
\end{cases}
\tag{59}
$$

We can see that the scheme (59) is a fully decoupled and linear scheme, but the added stabilization term in the latent heat contains the implicit processed potential ϕ^{n+1}, so it is necessary to solve the phase-field equation with variable coefficients at each time step. Moreover, due to the specific form of the stabilization term, the scheme (59) only has a first-order version so far and it is quite challenging to upgrade this scheme to the second-order version. Compared with the above scheme, the scheme (32)–(35) is linear, fully decoupled, second-order time-accurate, and unconditionally energy stable, which illustrates very high efficiency in practice.

3.4 | Unconditional energy stability

Next, we prove the scheme (32)–(35) complies with the energy dissipation structure, as shown below.

Theorem 1. *The time-discrete scheme (32)–(35) satisfies the discrete energy dissipation law as follows*

$$
\frac{1}{\delta t}(E^{n+1} - E^n) \le -\frac{\lambda D}{\epsilon K}\|\nabla T^{n+1}\|^2 - \tau\left\|\frac{3\phi^{n+1} - 4\phi^n + \phi^{n-1}}{2\delta t}\right\|^2 \le 0,
\tag{60}
$$

where $E^{n+1} \ge 0$ that is defined as

$$
\begin{aligned}
E^{n+1} = {} & \frac{1}{2}\left(\frac{1}{2}|U^{n+1}|^2 + \frac{1}{2}|2U^{n+1} - U^n|^2\right) + \frac{\lambda}{2\epsilon K}\left(\frac{1}{2}\|T^{n+1}\|^2 + \frac{1}{2}\|2T^{n+1} - T^n\|^2\right) \\[2mm]
& + \frac{\lambda}{2\epsilon}\left(\frac{1}{2}|Q^{n+1}|^2 + \frac{1}{2}|2Q^{n+1} - Q^n|^2\right) + \frac{C_1}{2}\left(\frac{1}{2}\|\nabla\phi^{n+1}\|^2 + \frac{1}{2}\|\nabla(2\phi^{n+1} - \phi^n)\|^2\right) \\[2mm]
& + \frac{C_2}{2\epsilon^2}\left(\frac{1}{2}\|\phi^{n+1}\|^2 + \frac{1}{2}\|2\phi^{n+1} - \phi^n\|^2\right).
\end{aligned}
\tag{61}
$$

Proof. First, it is easy to derive the following identity

$$
2a(3a - 4b + c) = a^2 + (2a - b)^2 - b^2 - (2b - c)^2 + (a - 2b + c)^2,
\tag{62}
$$

which will be repeatedly used.

By taking the L^2 inner product of (32) with $\frac{1}{2}(3\phi^{n+1} - 4\phi^n + \phi^{n-1})$, and using (62), we obtain

$$
\begin{aligned}
\tau\delta t\| & \frac{3\phi^{n+1} - 4\phi^n + \phi^{n-1}}{2\delta t}\|^2 \\
& + \frac{C_1}{2}\left(\left(\frac{1}{2}\|\nabla\phi^{n+1}\|^2 + \frac{1}{2}\|2\nabla\phi^{n+1} - \nabla\phi^n\|^2\right) - \left(\frac{1}{2}\|\nabla\phi^n\|^2 + \frac{1}{2}\|2\nabla\phi^n - \nabla\phi^{n-1}\|^2\right)\right) \\
& + \frac{C_2}{2\epsilon^2}\left(\left(\frac{1}{2}\|\phi^{n+1}\|^2 + \frac{1}{2}\|2\phi^{n+1} - \phi^n\|^2\right) - \left(\frac{1}{2}\|\phi^n\|^2 + \frac{1}{2}\|2\phi^n - \phi^{n-1}\|^2\right)\right) \\
& + \frac{C_1}{4}\|\nabla\phi^{n+1} - 2\nabla\phi^n + \nabla\phi^{n-1}\|^2 + \frac{C_2}{4\epsilon^2}\|\phi^{n+1} - 2\phi^n + \phi^{n-1}\|^2 \\
= & -\frac{1}{2}U^{n+1}\int_\Omega H^*(3\phi^{n+1} - 4\phi^n + \phi^{n-1})d\boldsymbol{x} \\
& \underbrace{- \frac{\lambda}{2\epsilon}Q^{n+1}\int_\Omega p(\phi^*)T^*(3\phi^{n+1} - 4\phi^n + \phi^{n-1})d\boldsymbol{x}}_{I_1}.
\end{aligned}
\tag{63}
$$

By multiplying (33) with U^{n+1}, we get

$$
\begin{aligned}
\left(\frac{1}{2}|U^{n+1}|^2 + \frac{1}{2}|2U^{n+1} - U^n|^2\right) - \left(\frac{1}{2}|U^n|^2 + \frac{1}{2}|2U^n - U^{n-1}|^2\right) \\
+ \frac{1}{2}|U^{n+1} - 2U^n + U^{n-1}|^2 = \frac{1}{2}U^{n+1}\int_\Omega H^*(3\phi^{n+1} - 4\phi^n + \phi^{n-1})d\boldsymbol{x}.
\end{aligned}
\tag{64}
$$

By taking the L^2 inner product of (34) with $\delta t\frac{\lambda}{\epsilon K}T^{n+1}$, we obtain

$$
\begin{aligned}
\frac{\lambda}{2\epsilon K}\left(\frac{1}{2}\|T^{n+1}\|^2 + \frac{1}{2}\|2T^{n+1} - T^n\|^2\right) - \frac{\lambda}{2\epsilon K}\left(\frac{1}{2}\|T^n\|^2 + \frac{1}{2}\|2T^n - T^{n-1}\|^2\right) \\
+ \frac{\lambda}{4\epsilon K}\|T^{n+1} - 2T^n + T^{n-1}\|^2 + \frac{\lambda D}{\epsilon K}\delta t\|\nabla T^{n+1}\|^2 \\
= \underbrace{\delta t\frac{\lambda}{\epsilon}Q^{n+1}\int_\Omega p(\phi^*)\phi_t^* T^{n+1}d\boldsymbol{x}}_{II_1}.
\end{aligned}
\tag{65}
$$

By multiplying (35) with $\delta t\frac{\lambda}{\epsilon}Q^{n+1}$, we get

$$
\begin{aligned}
\frac{\lambda}{2\epsilon}(\frac{1}{2}|Q^{n+1}|^2 + \frac{1}{2}|2Q^{n+1} - Q^n|^2) - \frac{\lambda}{2\epsilon}(\frac{1}{2}|Q^n|^2 + \frac{1}{2}|2Q^n - Q^{n-1}|^2) \\
+ \frac{\lambda}{4\epsilon}|Q^{n+1} - 2Q^n + Q^{n-1}|^2 \\
= \underbrace{\frac{\lambda}{2\epsilon}Q^{n+1}\int_\Omega p(\phi^*)T^*(3\phi^{n+1} - 4\phi^n + \phi^{n-1})d\boldsymbol{x}}_{I_2} \\
\underbrace{- \delta t\frac{\lambda}{\epsilon}Q^{n+1}\int_\Omega p(\phi^*)\phi_t^* T^{n+1}d\boldsymbol{x}}_{II_2}.
\end{aligned}
\tag{66}
$$

By combining (63)–(66) and noting I_1 and I_2, II_1 and II_2 are canceled, we obtain

$$
\begin{aligned}
\left(\frac{1}{2}|U^{n+1}|^2 + \frac{1}{2}|2U^{n+1} - U^n|^2\right) - \left(\frac{1}{2}|U^n|^2 + \frac{1}{2}|2U^n - U^{n-1}|^2\right) \\
+ \frac{\lambda}{2\epsilon K}\left(\frac{1}{2}\|T^{n+1}\|^2 + \frac{1}{2}\|2T^{n+1} - T^n\|^2\right) - \frac{\lambda}{2\epsilon K}\left(\frac{1}{2}\|T^n\|^2 + \frac{1}{2}\|2T^n - T^{n-1}\|^2\right)
\end{aligned}
$$

$$+ \frac{\lambda}{2\epsilon} \left(\frac{1}{2}|Q^{n+1}|^2 + \frac{1}{2}|2Q^{n+1} - Q^n|^2 \right) - \frac{\lambda}{2\epsilon} \left(\frac{1}{2}|Q^n|^2 + \frac{1}{2}|2Q^n - Q^{n-1}|^2 \right)$$

$$+ \frac{C_1}{2} \left(\left(\frac{1}{2}\|\nabla\phi^{n+1}\|^2 + \frac{1}{2}\|2\nabla\phi^{n+1} - \nabla\phi^n\|^2 \right) - \left(\frac{1}{2}\|\nabla\phi^n\|^2 + \frac{1}{2}\|2\nabla\phi^n - \nabla\phi^{n-1}\|^2 \right) \right)$$

$$+ \frac{C_2}{2\epsilon^2} \left(\left(\frac{1}{2}\|\phi^{n+1}\|^2 + \frac{1}{2}\|2\phi^{n+1} - \phi^n\|^2 \right) - \left(\frac{1}{2}\|\phi^n\|^2 + \frac{1}{2}\|2\phi^n - \phi^{n-1}\|^2 \right) \right)$$

$$+ \left\{ \frac{C_1}{4}\|\nabla\phi^{n+1} - 2\nabla\phi^n + \nabla\phi^{n-1}\|^2 + \frac{C_2}{4\epsilon^2}\|\phi^{n+1} - 2\phi^n + \phi^{n-1}\|^2 \right.$$

$$+ \frac{1}{2}|U^{n+1} - 2U^n + U^{n-1}|^2 + \frac{\lambda}{4\epsilon K}\|T^{n+1} - 2T^n + T^{n-1}\|^2$$

$$\left. + \frac{\lambda}{4\epsilon}|Q^{n+1} - 2Q^n + Q^{n-1}|^2 \right\}$$

$$= -\frac{\lambda D}{\epsilon K}\delta t\|\nabla T^{n+1}\|^2 - \tau\delta t\|\frac{3\phi^{n+1} - 4\phi^n + \phi^{n-1}}{2\delta t}\|^2. \tag{67}$$

Finally, we obtain (60) from (67) after dropping the positive terms in {}. ∎

4 | NUMERICAL SIMULATIONS

In this section, we first implement several numerical examples to verify the energy stability and convergence rate of the proposed decoupled scheme using scalar auxiliary variables (32)–(35) (abbreviated as DSAV scheme, for short). Then we perform numerical simulations of fourfold and sixfold crystal growth examples in 2D and 3D, to show the effectiveness of the scheme. In all the examples below, we set the computational domain to be a rectangular domain of $[0, 2\pi]^d$, $d = 2, 3$. For directions with periodic boundary conditions, we use the Fourier spectral method to discretize them. For the directions with boundary conditions specified in (37), we use the Legendre–Galerkin method for spatial discretizations (cf. Reference 46).

4.1 | Stability tests

In this subsection, we perform several stability tests in 2D to verify the unconditional energy stability of the scheme DSAV (32)–(35). We set the initial condition of ϕ to be a circular shape given as follows:

$$\phi^0(x, y) = \tanh\left(\frac{1.5 - \sqrt{(x - \pi)^2 + (y - \pi)^2}}{\epsilon}\right), T^0(x, y) = 0. \tag{68}$$

The computational domain is set to $\Omega = [0, 2\pi]^2$. For the x-direction, we set periodic boundary conditions, and use the Fourier-spectral method with 257 Fourier modes for discretization. For the y-direction, we adopt the homogenous Neumann boundary conditions (37) and use the Legendre–Galerkin method and Legendre polynomials up to 256 degrees for discretization. Hence the interface can be well resolved using a sufficiently fine mesh. We use the fourfold anisotropic coefficient (4) and set the model parameters as

$$\tau = 1, \lambda = 1, D = 2.25e - 1, \epsilon = 8e - 2, K = 1, \epsilon_4 = 0.25, B = 10. \tag{69}$$

We first verify whether the developed scheme maintains energy stability by plotting the time evolution of the total free energy (61) using different time steps. Since the scheme DSAV contains two stabilizers (C_i, $i = 1, 2$), in order to verify if they are effective in enhancing stability, we compare the following two sets of parameters:

$$\text{(I) } C_1 = C_2 = 0; \quad \text{(II) } C_1 = 0.5, C_2 = 4. \tag{70}$$

In the parameter set (I), we set the parameter C_i vanished; in contrast, in the parameter set (II), we set the parameter C_1 as large as possible and $C_2 \sim O(1)$ to testify their effects on stability in practice.

- First, we use the parameter set given in (I) and adopt a time step of $\delta t = 0.01$. The computed energy curve blows up quickly, as shown in Figure 1(A). We again adopt a smaller time step of $\delta t = 1e-6$, but the results obtained are not improved, and the energy curve obtained still explodes quickly, as shown in Figure 1(B). This means energy stability is not obtained when $C_i = 0$.

- Then, we use the parameter set given in (II) and plot energy curves using various time steps in Figure 2(A). The energy curves obtained indicate very good monotonic attenuation which means that the parameters C_i can effectively stabilize the computations. For this particular example, when C_i are absent, we still cannot get stable stability results even if the time step is as small as $\delta t = 1e-6$. Besides, in Figure 2(B), we plot the time evolution of the value of the auxiliary variable Q using different time steps. We find that the size of Q is always close to 1, which means that the sum of the two integral terms in (35) is close to 0.

Finally, we implement the scheme by using the time step of $\delta t = 0.01$ till the steady-state. Snapshots of the configurations of ϕ at different times are shown in Figure 3. We find that due to the imposed fourfold anisotropy, the circular interface gradually evolves into a rhombus.

4.2 | Accuracy tests

In this subsection, we further perform some convergence tests on the isotropic case ($\epsilon_4 = 0$) and the anisotropic case ($\epsilon_4 \neq 0$). We still set the 2D computational domain as $\Omega = [0, 2\pi]^2$ and assume the periodic boundary conditions along the x-direction and homogenous Neumann boundary conditions (37) along the y-direction. 257 Fourier modes are used to discretize x-direction and the Legendre polynomials with degrees up to 256 are used for the y-direction.

For the isotropic case, we assume that the exact solutions of the system (6)–(7) are given by

$$\phi(x, y, t) = \sin(x)\cos(y)\cos(t), \quad T(x, y, t) = \cos(x)\cos(y)\cos(t), \tag{71}$$

and apply some suitable force fields so that the given solutions in (71) satisfy the system. The model parameters are set as

$$\tau = 5000, \lambda = 300, D = 2e-4, \epsilon = 1.2e-2, K = 1,$$
$$\epsilon_4 = 0, B = 10, C_1 = 0.5, C_2 = 4, \tag{72}$$

where the stability parameters C_i come from (II) in (70). In Figure 4(A), we plot the numerical errors of L^2 at $t = 1$ of the two unknown variables ϕ and T by using various time steps between the obtained numerical solution and the given exact solution (71). We observe that the scheme provides almost perfect second-order accuracy for both variables.

For the anisotropic case, we test the convergence rate by performing mesh refinement in time. We use the initial conditions given in (68) and the model parameters given in (69). We still use the stability parameters (II) of (70) because it can balance the stability and numerical errors well. Since the exact solutions are not known yet, we choose the numerical solutions computed by the scheme with a very tiny time step size $\delta t = 1e-9$ as the exact solution. In Figure 4(B), we plot the L^2 errors of two unknown variables between the numerical solution and the exact solution at $t = 0.2$ where the time step δt is varied from $\delta t = 0.01$ to $\delta t = \frac{0.01}{2^5}$ with a factor of $1/2$. The computed results show the expected second-order of accuracy for ϕ and T.
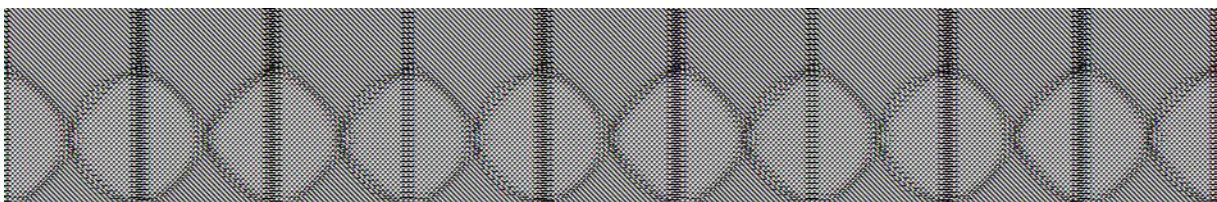

FIGURE 3 The configuration profiles of the phase-field variable ϕ computed using the developed scheme. Snapshots are taken at $t = 0$, 0.05, 0.1, 0.2, 0.3, and 0.8, where the initial conditions are given in (68) and the time step is $\delta t = 1e-2$

Next, we use the above mesh refinement example to compare the computational efficiency of the proposed DSAV scheme and other versions of schemes.

- The first scheme we compare is the so-called first-order explicit-type scheme, which is usually used in computational material science (abbreviated as Exp, see[47]), where the time derivative is discretized by backward Euler method and nonlinear terms are discretized in an explicit way. In Figure 4(C), we compare the order of accuracy computed by the schemes DSAV and Exp with various time steps. Since the scheme Exp is not unconditionally energy stable, we find that when the time step is large, it blows up and thus the error points are missed. When δt is extremely small, the scheme Exp shows the first-order accuracy. For this particular mesh refinement example, numerical tests show that the running time using the scheme Exp is about 1/2 of the running time of the scheme DSAV per time step. Therefore, if the allowable error is around $O(1e-4)$, then the maximum time step allowed by Exp is about $\delta t = 1e-5$, while the time step allowed by DSAV is about $\delta t = 5e-3$. This means that under the same magnitude of accuracy, the DSAV scheme is 250 times faster than the scheme Exp.
- The second scheme we compare is the IEQ scheme developed in Reference 15 (abbreviated as IEQ). This is also a second-order time marching scheme, but it has to solve a fully coupled elliptic system with variable coefficients at each time step. In Figure 4(D), we compare the accuracy order computed by the schemes DSAV and IEQ. They all present second-order accuracy, and magnitude of error of each δt is almost the same. However, after comparing the number
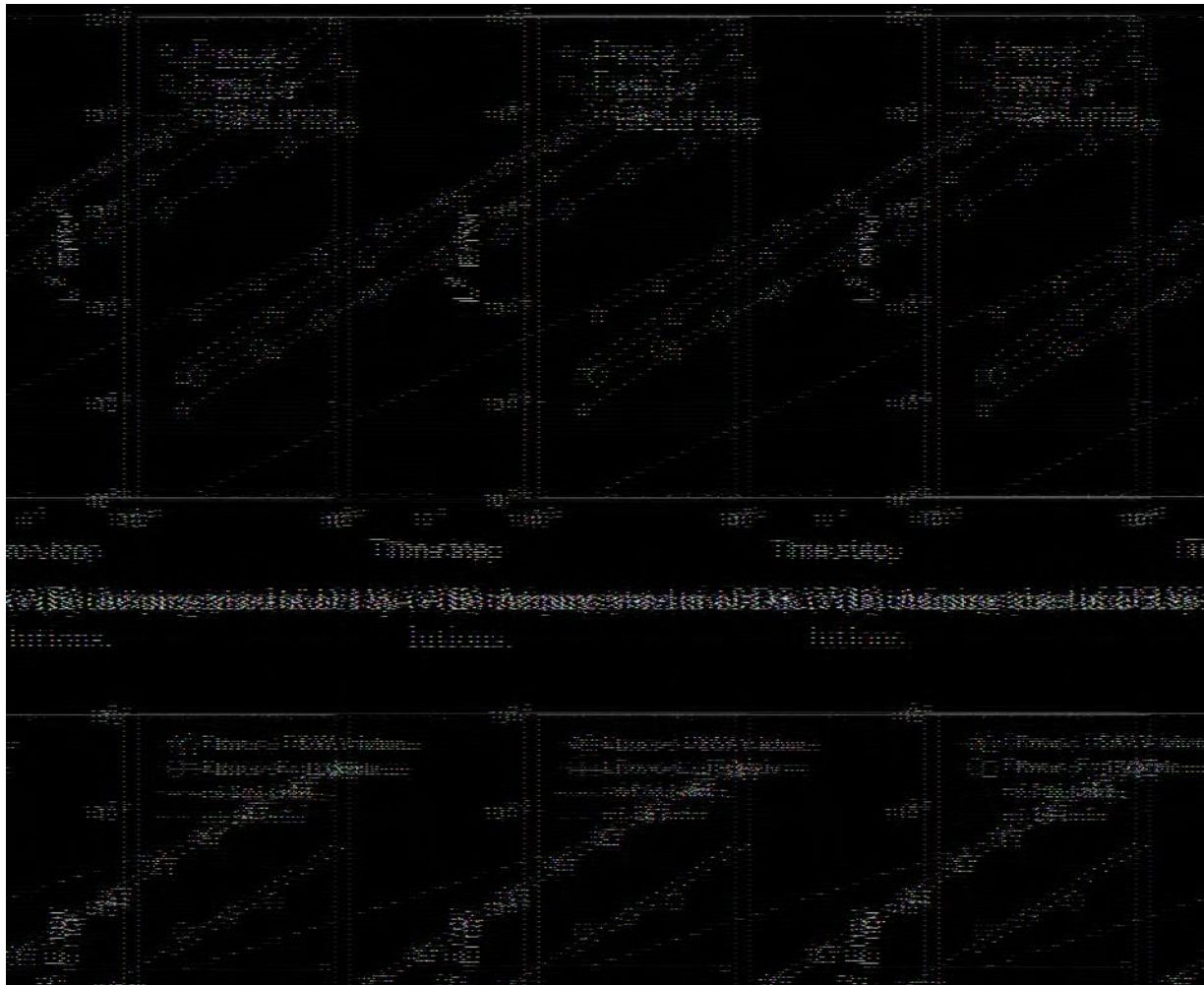

FIGURE 4 (A) Accuracy tests with the presumed exact solutions given in (71); (B) accuracy tests by refining the time steps with the initial conditions given in (68); (C) the comparison of accuracy computed by the schemes: DSAV and Exp; and (D) the comparisons of accuracy and number of iterations computed by the schemes: DSAV and IEQ. (In (A) and (B), the L^2 numerical errors of ϕ and T using various time steps are plotted. In (C) and (D), the L^2 numerical errors of ϕ using various time steps are plotted.)

of iterations needed for both schemes (which is appended as a small inset figure in Figure 4(D)), we immediately find the scheme DSAV is much more efficient than IEQ. For example, when $\delta t = 0.01$, the number of iterations required by IEQ is around 60, while the scheme DSAV just need 5 iterations since it only needs to solve five decoupled elliptic equations with constant coefficients. This means the scheme DSAV is 12 times faster than IEQ when $\delta t = 0.01$.

4.3 ⎸ Fourfold crystal growth in 2D and 3D

In this subsection, using the fourfold anisotropy, we focus on simulating the dynamic process of heterogeneous growth of small crystal nuclei in 2D and 3D spaces and studying how the latent heat coefficient K affects the shape of dendrites.

For 2D, we set the computational domain to be $\Omega = [0, 2\pi]^2$ and the initial condition of ϕ to be a circular kernel, as shown below:

$$\phi^0(x, y) = \tanh\left(\frac{\sqrt{r - (x - \pi)^2 + (y - \pi)^2}}{0.022}\right), T^0(x, y) = \begin{cases} 0, & \phi^0(x, y) > 0; \\ -0.55, & \text{otherwise,} \end{cases} \tag{73}$$

with $r = 0.105$. We assume that the system satisfies the homogeneous Neumann boundary conditions (37) and use the Legendre–Galerkin method to discretize the space. The Legendre polynomials with degrees up to 512 are adopted for each direction. The model parameters are set as

$$\lambda = 355, D = 2.25\mathrm{e} - 4, \tau = D^{-1}, \epsilon = 1.12\mathrm{e} - 2,$$
$$\epsilon_4 = 0.05, B = 10, C_1 = 0.9, C_2 = 4, \delta t = 0.01. \tag{74}$$

The parameter K is varied in the next simulations.

In Figure 5(A) with $K = 0.5$, from the snapshots of ϕ at different times, we find that the crystal phase eventually grows into an anisotropic rhombus with four concave sides due to anisotropic effects. In Figure 5(B–D), we increase the values of K from 0.6 to 0.8 with an incremental value of 0.1. It can be seen from the profile of the variable ϕ that four prominent branches are always formed, and the parameter K affects the width of the branch. When K becomes larger, the width of the branch becomes thinner and the tip becomes sharper. In Figure 5(E), we show the configuration profile of the temperature T at the last moment of each simulation. Because the latent heat coupling term restricts heat to propagate only at the liquid–solid interface, the contour of T is very consistent with interface contour described by the phase-field variable ϕ.

We continue to perform 3D simulations. The computed domain is set as $(x, y, z) \in \Omega = [0, 2\pi]^3$, and the initial conditions read as (shown in the first subfigure of Figure 6(A)):

$$\phi^0(x, y, z) = \tanh\left(\frac{\sqrt{r - (x - \pi)^2 + (y - \pi)^2 + (z - \pi)^2}}{0.022}\right),$$

$$T^0(x, y, z) = \begin{cases} 0, & \phi^0(x, y, z) > 0; \\ -0.55, & \text{otherwise,} \end{cases} \tag{75}$$

with $r = 0.105$. We set the model parameters as

$$\lambda = 355, D = 3.5\mathrm{e} - 2, \tau = 4.4e2, \epsilon = 4.5\mathrm{e} - 2,$$
$$\epsilon_4 = 0.05, B = 10, C_1 = 0.9, C_2 = 4, \delta t = 0.01. \tag{76}$$

We assume the periodic boundary conditions followed by the x- and y-directions which are then discretized by using 129^2 Fourier-modes. For the z-direction, we use the homogeneous Neumann boundary conditions and discretize it by using the Legendre–Galerkin method with the Legendre polynomials of degrees up to 128.

In Figure 6(A–E), we display the crystal configurations at different times by plotting the crystal isosurface $\{\phi = 0\}$, where the parameter K is changed from 0.5 to 2.5 with an incremental value of 0.5. In each simulation, we observe the formation of six protruding branches distributed in the top, bottom, left, right, front, and back over time. As K increases,
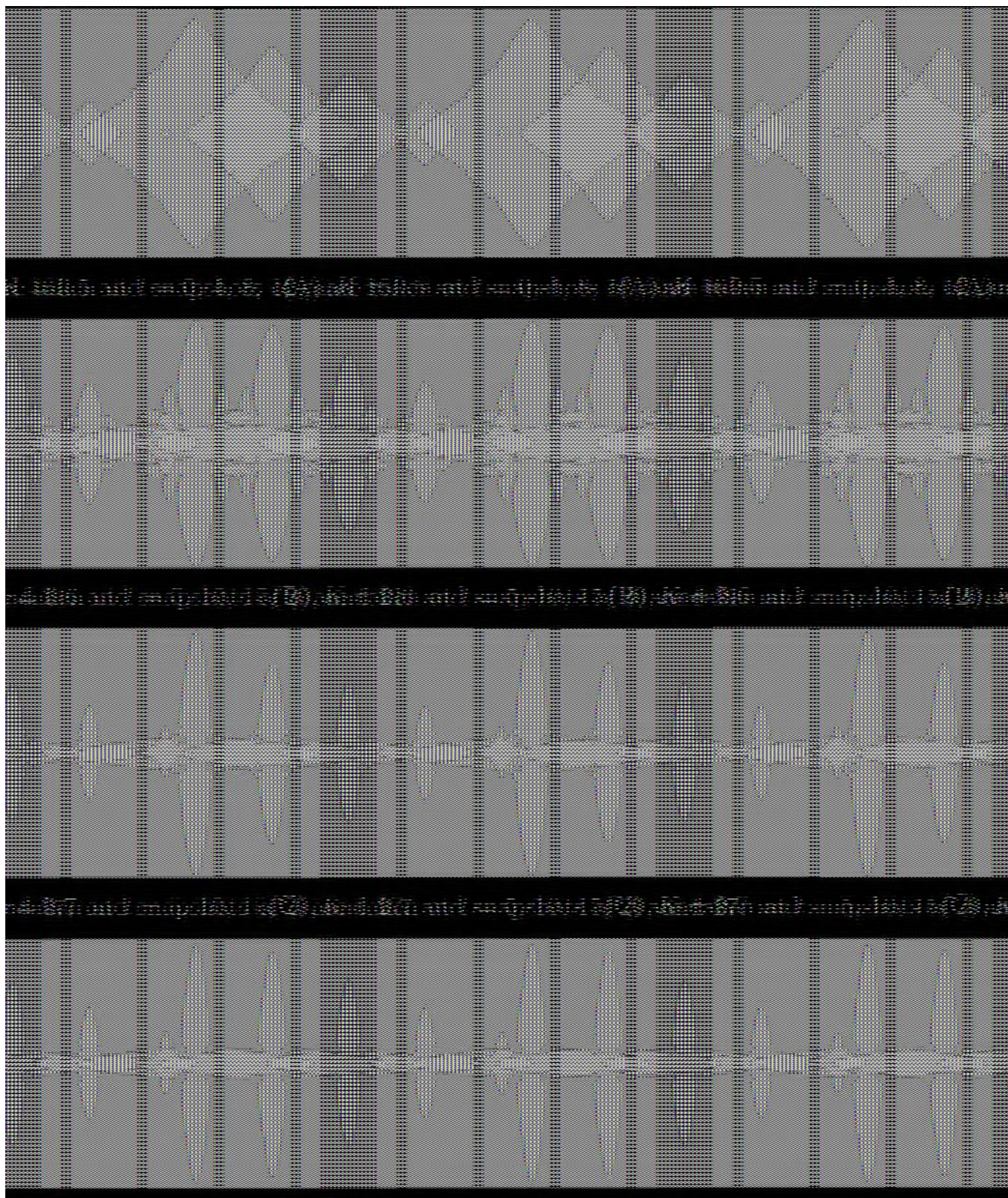
FIGURE 5   2D dendritic crystal growth with fourfold anisotropy by varying the parameter K. From (A) to (D), the parameter K is 0.5, 0.6, 0.7, and 0.8, where each simulation takes snapshots of ϕ at different times, and (E) the profile of the temperature T displayed at last moment in each 2D simulation

FIGURE 6 3D dendritic crystal growth with fourfold anisotropy by varying the parameter K. From (A) to (E), the parameter K is 0.5, 1, 1.5, 2, and 2.5 where each simulation takes snapshots of the crystal isosurface $\{\phi = 0\}$ at different times
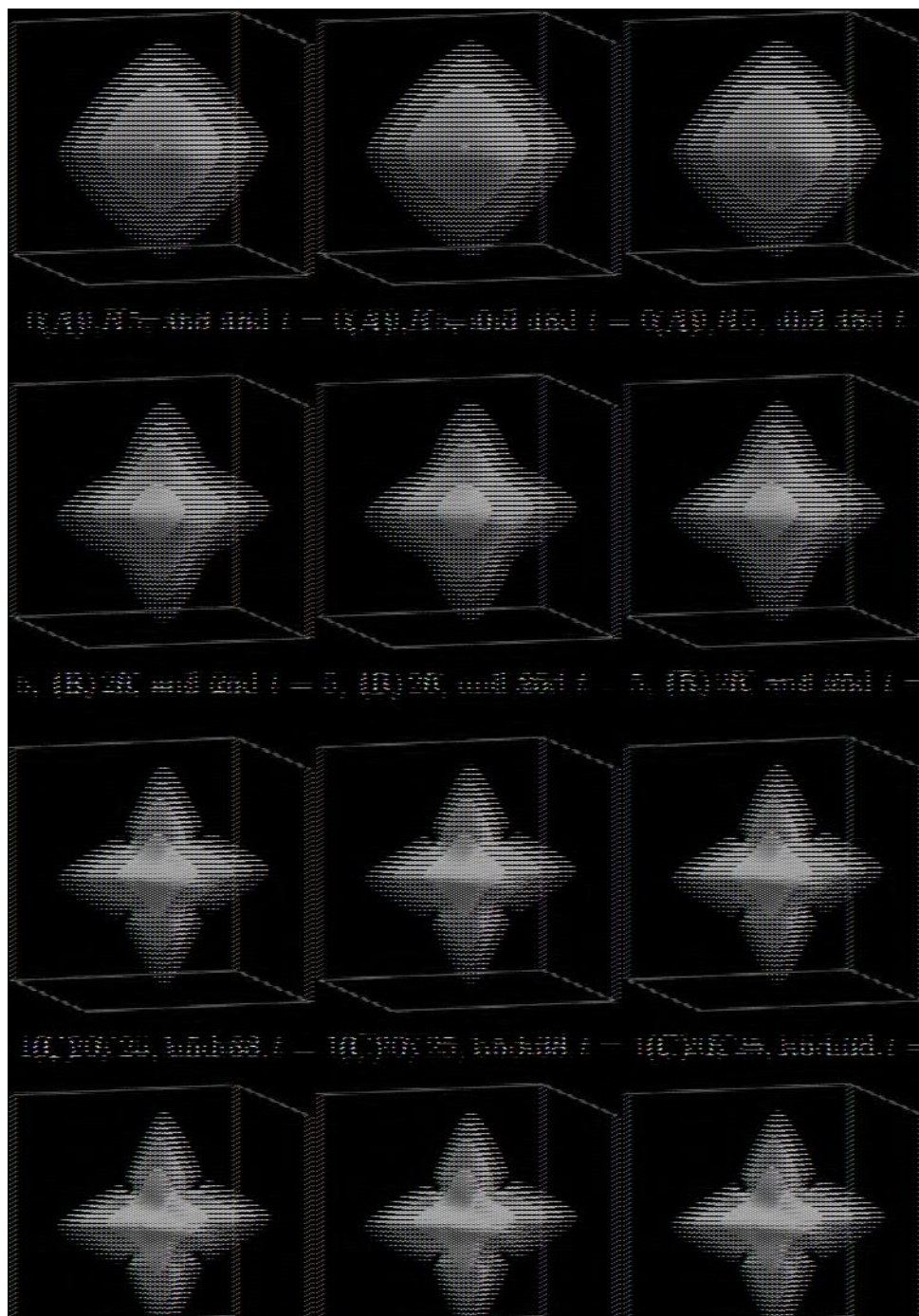
the formed branch gradually becomes thinner and its pointed tip becomes sharper. In Figure 7(A,B), we plot the evolution curves of the logarithm of the total free energy, the area/volume of the crystal ($\int_{\Omega} \frac{1+\phi}{2} d\boldsymbol{x}$) for all 2D and 3D simulations. It can be seen that with time, the free energy exhibits a monotonic decay, and the area/volume exhibits a monotonic increase.

4.4 | Sixfold crystal growth in 2D and 3D

In this subsection, by setting $m = 6$ in (3), we simulate the dynamic process of heterogeneous growth of small crystal nuclei in 2D and 3D spaces affected by the sixfold anisotropy. We still investigate how the latent heat coefficient of K affects the
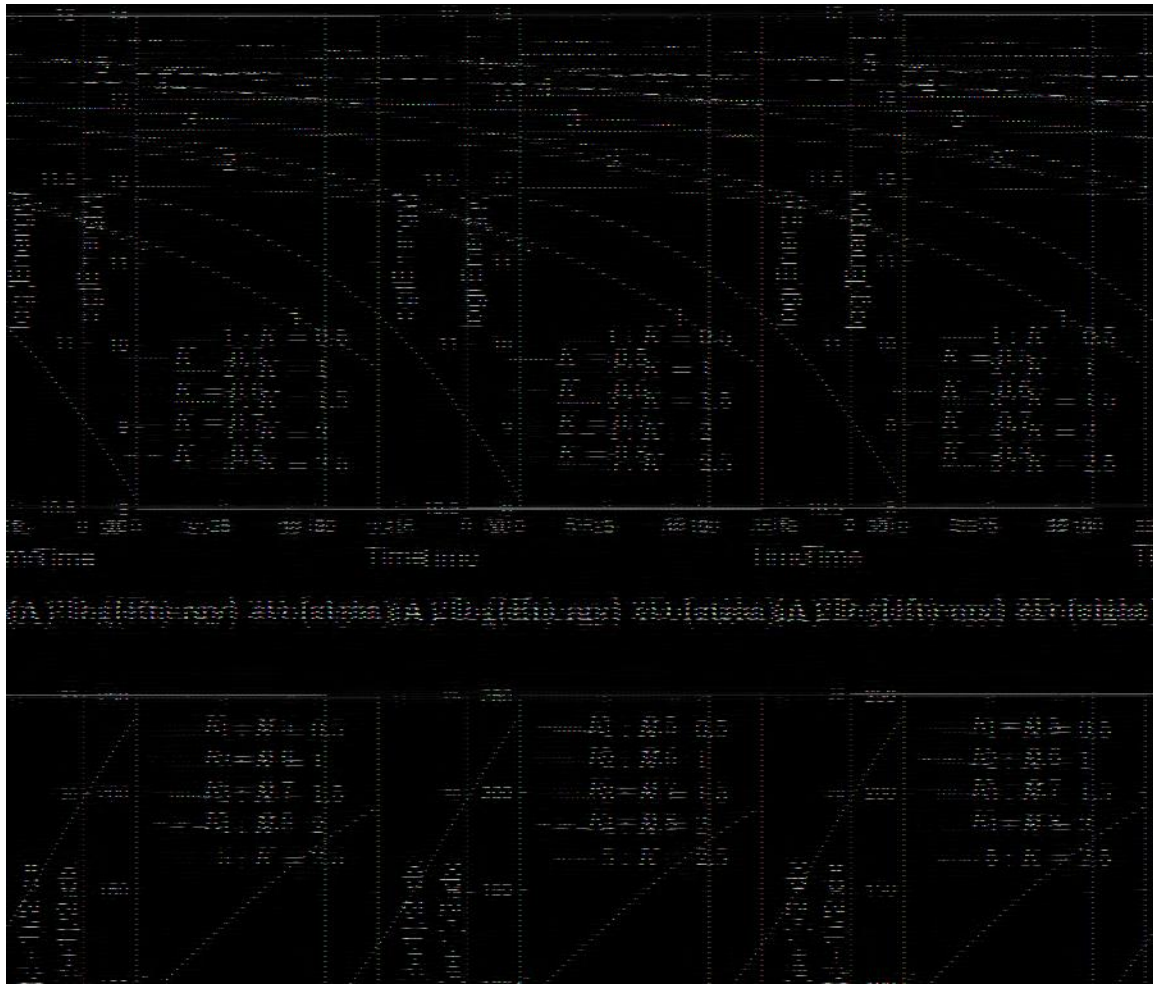
FIGURE 7 Time evolutions of (A) the logarithm of the total free energy functional (61), and (B) the crystal area/volume $\int_\Omega \frac{1+\phi}{2} d\boldsymbol{x}$, for all 2D and 3D simulations with the fourfold anisotropy
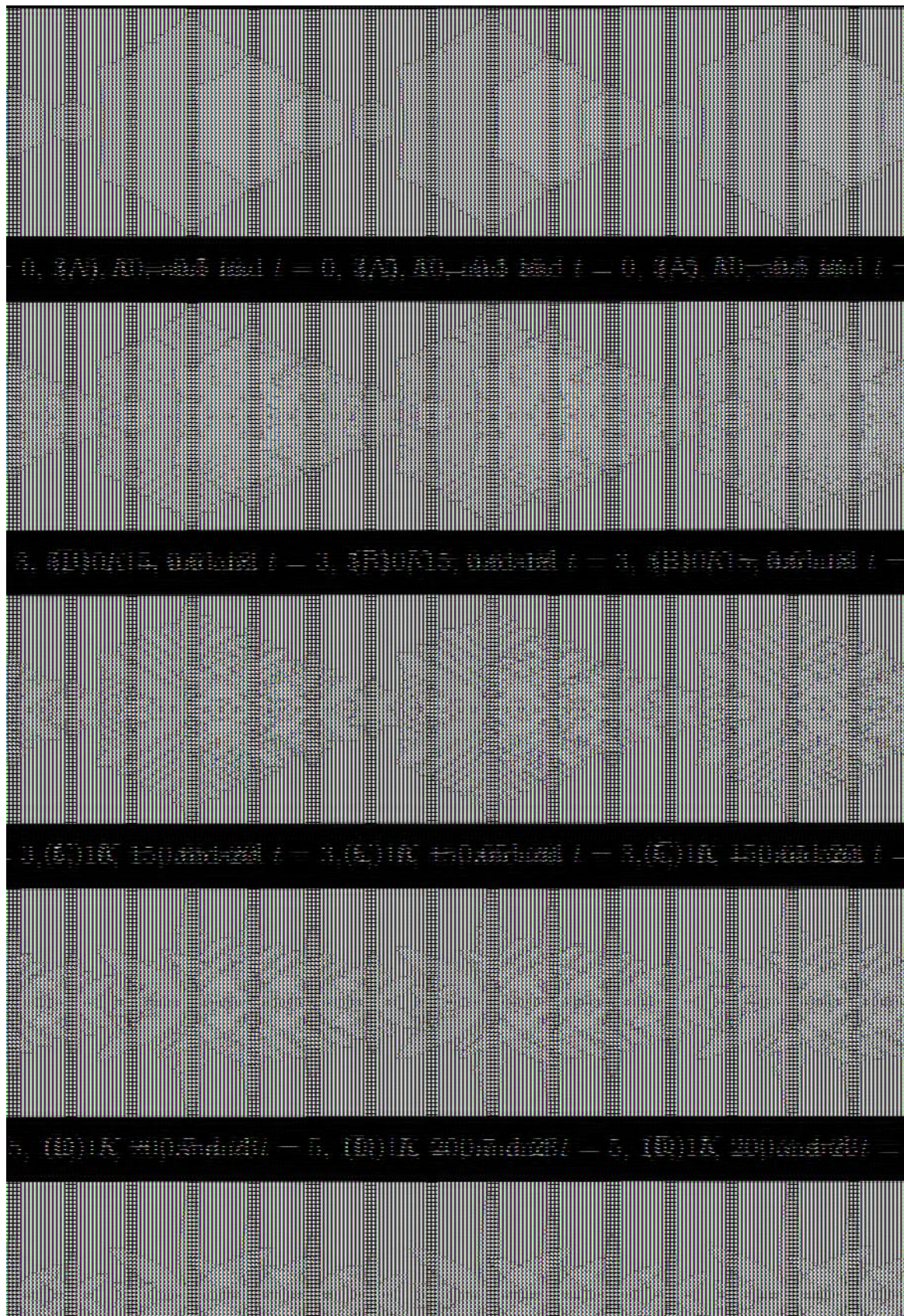
shape of the dendritic crystal. The computational domain and the initial conditions ϕ^0, T^0 are the same as the fourfold simulations in the previous example.

For 2D simulations, we assume that the system satisfies the homogeneous Neumann boundary conditions (37) and discretize the space using the Legendre–Galerkin method where Legendre polynomials with degrees up to 1024 are used for each direction. We set the parameters as

$$\lambda = 380, D = 2.25\text{e} - 3, \tau = D^{-1}, \epsilon = 1.12\text{e} - 2, \epsilon_4 = 0.05,$$
$$B = 10, C_1 = 0.9, C_2 = 4, \delta t = 0.01. \tag{77}$$

In Figure 8, by changing the latent heat parameter K from 0.5 to 0.75 with an incremental value of 0.05, we plot the profiles of ϕ at different times until one of the protrusive branches touches the boundary. When $K = 0.5$, as shown in Figure 8(A), the initial circular core grows into a hexagon shape. When $K = 0.55, 0.6, 0.65$ which are shown in Figure 8(B–D), respectively, we observe many small holes form inside the crystal and the snow-flake pattern is obtained. We recall that, in Reference 4, by calculating a dendritic crystal growth model that is slightly different from the model studied in this article, a similar snowflake shape had been obtained. When $K = 0.7$, as shown in Figure 8(E), all the small holes disappear and six thin protrusive branches are formed. In Figure 8(F), the profiles of the temperature T at the last moment of each simulation are shown and their contours are consistent with the liquid-solid interfaces as well.

We continue to perform 3D simulations. We assume periodic boundary conditions for the x- and y-directions and discretize them by using 257^2 Fourier-modes. For the z-direction, the homogeneous Neumann boundary conditions
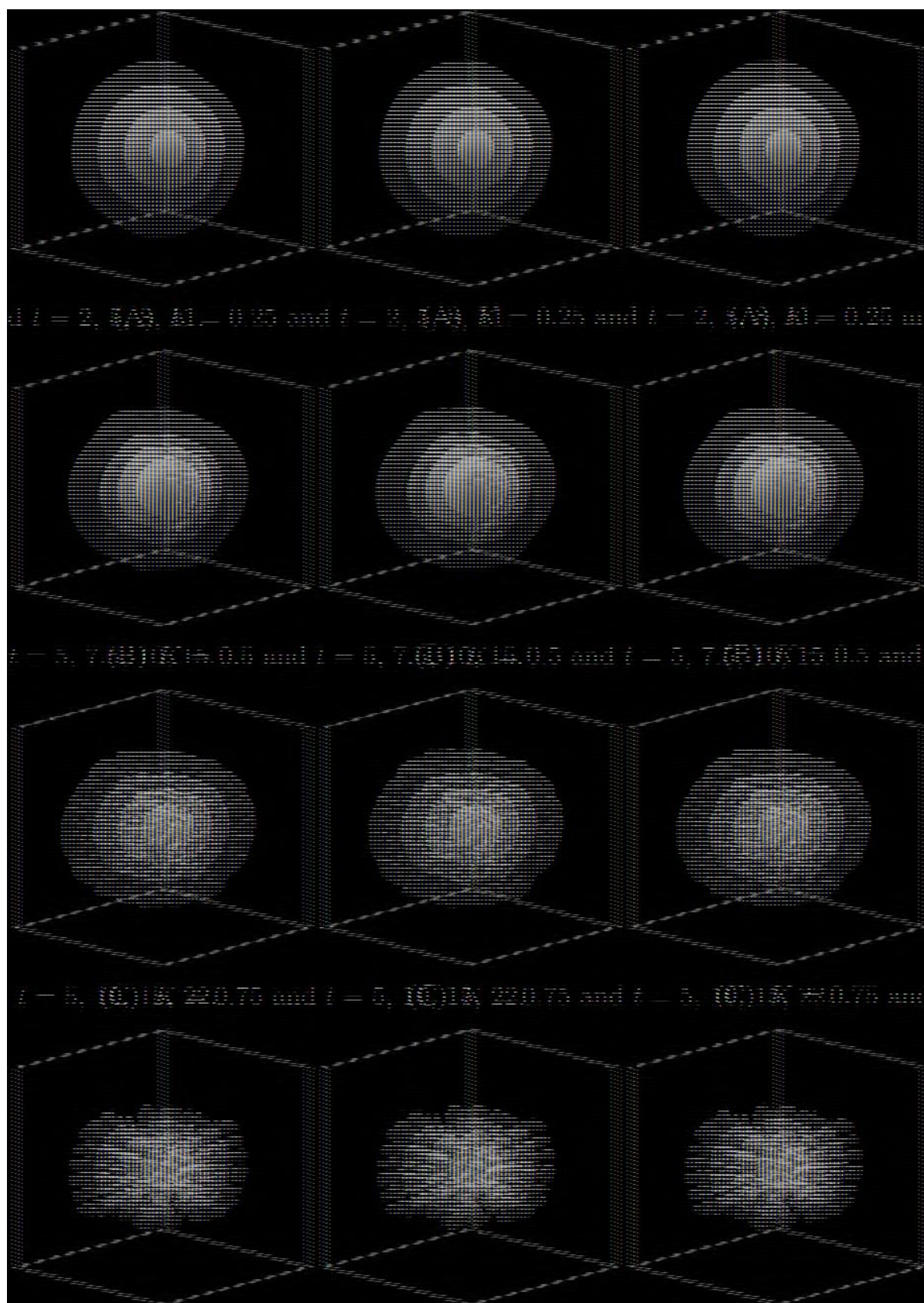
FIGURE 8 2D dendritic crystal growth with sixfold anisotropy by varying the parameter K. From (A) to (E), the parameter K is 0.5, 0.55, 0.6, 0.65, 0.7, 0.75, and 0.8, where each simulation takes snapshots of ϕ at different times. (E) The profile of the temperature T displayed at the last moment in each 2D simulation

FIGURE 9 3D dendritic crystal growth with sixfold anisotropy by varying the parameter K. From (A) to (D), the parameter *K* is 0.25, 0.5, 0.75, and 1.5 where each simulation takes snapshots of the crystal isosurface {$\phi = 0$} at different times, and (E) the crystal isosurface {$\phi = 0$} plotted by taking the top view where each displayed snapshot corresponds to the last moment of each simulation
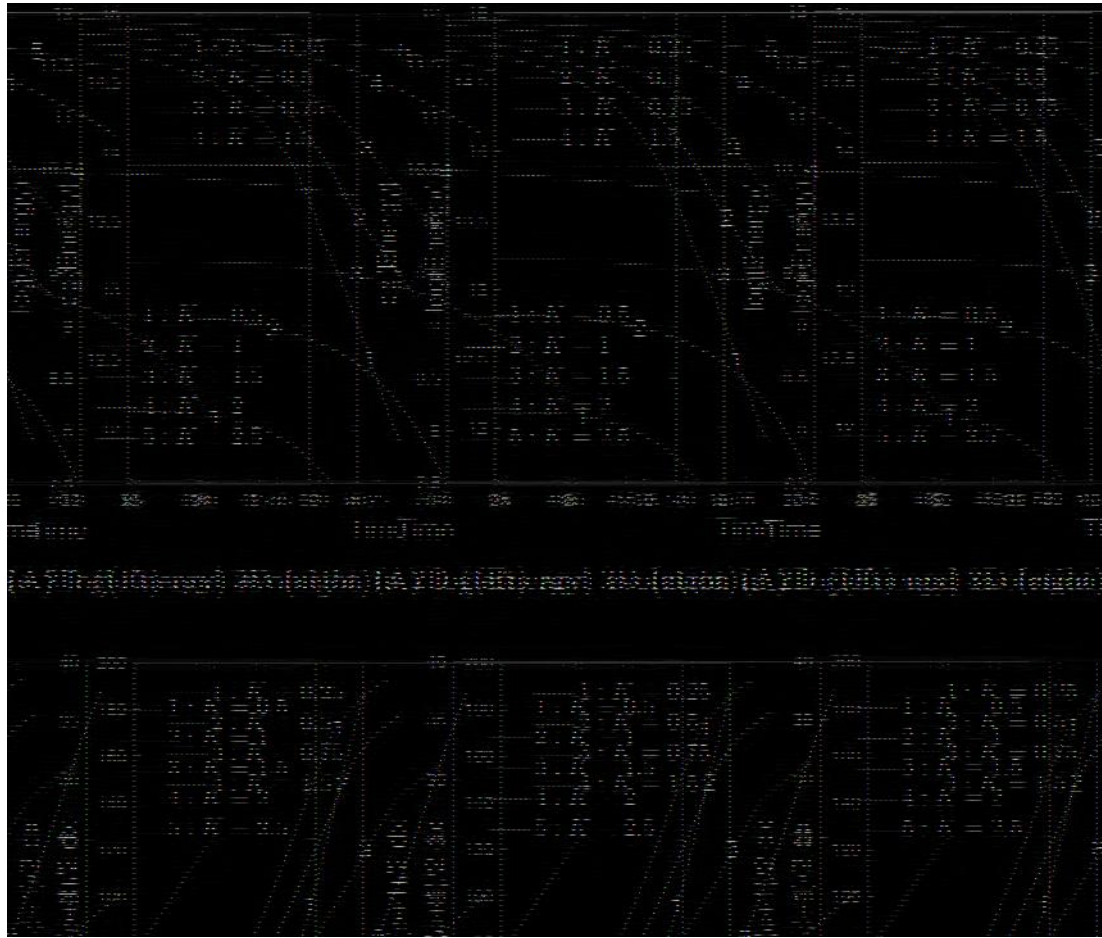
FIGURE 10 (A) Free energy evolutions by plotting the logarithm of (61), and (B) the crystal area/volume $\int_\Omega \frac{1+\phi}{2} dx$ evolutions over time, for all 2D and 3D simulations with the sixfold anisotropy

are adopted and the Legendre–Galerkin method with Legendre polynomials of degrees up to 256 is used. The model parameters are set as

$$\lambda = 380, D = 6.5\text{e} - 3, \tau = 4.4e2, \epsilon = 1.95\text{e} - 2, \epsilon_4 = 0.05,$$
$$B = 10, C_1 = 0.9, C_2 = 4, \delta t = 0.01. \tag{78}$$

In Figure 9(A–D), we show the dynamic growth of the crystal by drawing the isosurface $\{\phi = 0\}$ of the crystal at different times until the crystal touches the boundary. The parameter K is set to 0.25, 0.5, 0.75, and 1.5. As K increases, the shape of the crystal shows a rich and diverse structure, from the overall baseball to walnut with plenty of internal cavities. For example, when taking the side view, when $K = 0.25$, the crystal is like a baseball; when $K = 0.5$ and 0.75, the walnut; and when $K = 1.5$, the pine fruit cone. To obtain a better understanding of the crystal shape, in Figure 9(E), we use the top view to draw the isosurface of the formed crystal at the last moment of each simulation. From this particular perspective, we find that the 3D results are similar to the 2D results shown above. For example, when $K = 0.5$, the crystal appears as a hexagon; $K = 0.75, 1.5$, like snowflakes. In Figure 10, we plot the evolutions of the total free energy and the crystal area (2D)/volume (3D) ($\int_\Omega \frac{\phi+1}{2} dx$) for all 2D and 3D cases with the sixfold anisotropy.

5 | CONCLUDING REMARKS

In this article, for the highly coupled nonlinear phase-field dendritic growth model, we have developed a novel and very effective time-marching scheme to realize the fully decoupled structure and second-order accuracy in time. The

decoupling method makes full use of the "zero-energy-contribution" property of the coupled nonlinear terms. By simulating a large number of 2D and 3D benchmarking examples, such as the fourfold and sixfold anisotropic crystal formation, we have proved the stability and accuracy of the developed scheme. According to the author's knowledge, this developed scheme is the first to have almost all the desired properties, including linearity, second-order accuracy in time, full decoupling, and unconditional energy stability for the dendritic phase-field model. In addition, the decoupling technique can be used to deal with many nonlinear coupling models as long as the involved nonlinear coupling terms follow the "zero-energy-contribution" property, which indicates the generality of the method.

ACKNOWLEDGMENT

DATA AVAILABILITY STATEMENT

Data sharing is not applicable to this article as no datasets were generated or analyzed during the current study.

ORCID

Xiaofeng Yang 🔘 https://orcid.org/0000-0001-7382-3006

REFERENCES

1. Karma A, Rappel W. Phase-field model of dendritic sidebranching with thermal noise. *Phys Rev E*. 1999;60:3614-3625.
2. Karma A, Rappel W. Quantitative phase-field modeling of dendritic growth in two and three dimensions. *Phys Rev E*. 1998;57:4323-4349.
3. Collins JB, Levine H. Diffuse interface model of diffusion-limited crystal growth. *Phys Rev B*. 1985;31:6119.
4. Kobayashi R. Modeling and numerical simulations of dendritic crystal growth. *Physica D*. 1993;63:410.
5. Halperin BI, Hohenberg PC, Ma S-K. Renormalization-group methods for critical dynamics: I. recursion relations and effects of energy conservation. *Phys Rev B*. 1974;139(10):139–153.
6. Zhao Y, Li J, Zhao J, Wang Q. A linear energy and entropy-production-rate preserving scheme for thermodynamically consistent crystal growth models. *Appl Math Lett*. 2019;98:142-148.
7. Li J, Zhao J, Wang Q. Energy and entropy preserving numerical approximations of thermodynamically consistent crystal growth models. *J Comput Phys*. 2019;382:202-220.
8. Chen CC, Tsai YL, Lan CW. Adaptive phase field simulation of dendritic crystal growth in a forced flow:2d vs. 3d morphologies. *Int J Heat Mass Transf*. 2009;52:1158-1166.
9. Plapp M, Karma A. Multiscale finite-difference-diffusion-Monte-Carlo method for simulating dendritic solidification. *J Comput Phys*. 2000;165:592-619.
10. Shah A, Haider A, Shah S. Numerical simulation of two dimensional dendritic growth using phase field model. *World Journal of Mechanics*. 2014;4:128-136.
11. Warren JA, Boettinger WJ. Prediction of dentric growth and microsegregation patterns in a binary alloy using the phase field method. *Acta Metall Mater*. 1995;43:689-703.
12. Meca E, Shenoy V, Lowengrub J. Phase field modeling of two dimensional crystal growth with anisotropic diffusion. *Phys Rev E*. 2013;88:052409.
13. Karma A, Lobkovsky AE. Unsteady crack motion and branching in a phase-field model of brittle fracture. *Phys Rev Lett*. 2004;92:245510.
14. Zhao J, Wang Q, Yang X. Numerical approximations for a phase field dendritic crystal growth model based on the invariant energy quadratization approach. *Inter J Num Meth Engr*. 2017;110:279-300.
15. Yang X. Efficient linear, stabilized, second order time marching schemes for an anisotropic phase field dendritic crystal growth model. *Comput Meth Appl Mech Eng*. 2019;347:316-339.
16. Zhang J, Chen C, Yang X. A novel decoupled and stable scheme for an anisotropic phase-field dendritic crystal growth model. *Appl Math Lett*. 2019;95:122-129.
17. Zhang J, Yang X. A fully decoupled, linear and unconditionally energy stable numerical scheme for a melt-convective phase-field dendritic solidification model. *Comput Methods Appl Mech Eng*. 2020;363:112779.
18. Shen J, Yang X. The IEQ and SAV approaches and their extensions for a class of highly nonlinear gradient flow systems. *Contemp Math*. 2020;754:217-245.
19. Chen C, Yang X. Fast, provably unconditionally energy stable, and second-order accurate algorithms for the anisotropic Cahn-Hilliard model. *Comput Meth Appl Mech Eng*. 2019;351:35-59.
20. Yang X, Yu H. Efficient second order unconditionally stable schemes for a phase field moving contact line model using an invariant energy quadratization approach. *SIAM J Sci Comput*. 2018;40:B889-B914.
21. Abels H, Garcke H, Grün G. Thermodynamically consistent, frame indifferent diffuse interface models for incompressible two-phase flows with different densities. *Math Models Methods Appl Sci*. 2012;22:1150013.
22. Lev BI, Nazarenko VG, Nych AB, Tomchuk PM. Deformation and instability of nematic drops in an external electric field. *JETP Lett*. 2000;71:262-265.

23. Nochetto RH, Salgado AJ, Walker SW. A diffuse interface model for electrowetting with moving contact lines. *Math Models Methods Appl Sci*. 2014;24:67-111.

24. Nochetto RH, Salgado AJ, Tomas I. A diffuse interface model for two-phase ferrofluid flows. *Comput Meth Appl Mech Eng*. 2016;309:497-531.

25. Kobayashi R. A numerical approach to three-dimensional dendritic solidification. *Exp Math*. 1994;3:59-81.

26. Wang S-L, Sekerka RF, Wheeler AA, et al. Thermodynamically-consistent phase-field models for solidification. *Physica D*. 1993;69:189-200.

27. Shen J, Yang X. Numerical approximations of Allen–Cahn and Cahn–Hilliard equations. *Disc Cont Dyn Sys A*. 2010;28:1669-1691.

28. Eyre DJ. Unconditionally gradient stable time marching the Cahn-Hilliard equation. *Computational and Mathematical Models of Microstructural Evolution, volume 529 of Materials Research Society Symposium Proceedings*. San Francisco, CA: MRS; 1998:39-46.

29. Hu Z, Wise SM, Wang C, Lowengrub JS. Stable and efficient finite difference nonlinear-multigrid schemes for the phase field crystal equation. *J Comput Phys*. 2009;228:5323-5339.

30. Yang X. A novel fully-decoupled, second-order time-accurate, unconditionally energy stable scheme for a flow-coupled volume-conserved phase-field elastic bending energy model. *J Comput Phys*. 2021;432:110015.

31. Yang X. A new efficient Fully-decoupled and second-order time-accurate scheme for Cahn-Hilliard phase-field model of three-phase incompressible flow. *Comput Methods Appl Mech Eng*. 2021;376:13589.

32. Yang X. Numerical approximations of the Navier-Stokes equation coupled with volume-conserved multi-phase-field vesicles system: fully-decoupled, linear, unconditionally energy stable and second-order time-accurate numerical scheme. *Comput Methods Appl Mech Eng*. 2021;375:113600.

33. Yang X. A novel fully-decoupled, second-order and energy stable numerical scheme of the conserved Allen-Cahn type flow-coupled binary surfactant model. *Comput Methods Appl Mech Eng*. 2021;373:113502.

34. Yang X. A novel fully-decoupled scheme with second-order time accuracy and unconditional energy stability for the Navier-Stokes equations coupled with mass-conserved Allen-Cahn phase-field model of two-phase incompressible flow. *Int J Numer Methods Eng*. 2021;122:1283-1306.

35. Du Q, Nicolaides RA. Numerical analysis of a continuum model of phase transition. *SIAM J Numer Anal*. 1991;28:1310-1322.

36. Gomez H, van der Zee KG. Computational phase-field modeling. *Encyclopedia of Computational Mechanics*. 2nd ed. Hoboken, NJ: John Wiley & Sons, Ltd; 2017.

37. Gomez H, Calo VM, Bazilevs Y, Hughes TJR. Isogeometric analystis of the Cahn-Hilliard phase-field model. *Comput Methods Appl Mech Eng*. 2008;197:4333-4352.

38. Romero I. Thermodynamically consistent time stepping algorithms for nonlinear thermomechanical systems. *Int J Numer Meth Eng*. 2009;79:706-732.

39. Guermond J-L, Quartapelle L. A projection fem for variable density incompressible flows. *J Comput Phys*. 2000;165(4):167-188.

40. Guermond JL, Salgado A. A splitting method for incompressible flows with variable density based on a pressure Poisson equation. *J Comput Phys*. 2009;228(8):2834-2846.

41. Shen J, Yang X. A phase-field model and its numerical approximation for two-phase incompressible flows with different densities and viscositites. *SIAM J Sci Comput*. 2010;32:1159-1179.

42. Shen J, Yang X. Energy stable schemes for Cahn–Hilliard phase-field model of two-phase incompressible flows. *Chin Ann Math Ser B*. 2010;31(5):743-758.

43. Yang X. Linear, first and second order and unconditionally energy stable numerical schemes for the phase field model of homopolymer blends. *J Comput Phys*. 2016;327:294-316.

44. Han D, Wang X. A second order in time, uniquely solvable, unconditionally stable numerical scheme for Cahn–Hilliard–Navier–Stokes equation. *J Comput Phys*. 2015;290:139-156.

45. Shen J, Yang X. Decoupled energy stable schemes for phase-field models of two-phase complex fluids. *SIAM J Sci Comput*. 2014;36(1):B122-B145.

46. Shen J, Tang T, Wang L-L. *Spectral Methods: Algorithms, Analysis and Applications*. Berlin/Heidelberg, Germany: Springer; 2013.

47. Chen LQ, Shen J. Applications of semi-implicit Fourier-spectral method to phase-field equations. *Comput Phys Commun*. 1998;108:147-158.